Evaluation of the Potential for Wintertime Quantitative Precipitation Forecasting over Mountainous Terrain with an Explicit Cloud Model. Part I: Two-Dimensional Sensitivity Experiments

MICHAEL P. MEYERS AND WILLIAM R. COTTON

Colorado State University, Department of Atmospheric Science, Fort Collins, Colorado

(Manuscript received 21 August 1990, in final form 2 February 1991)

ABSTRACT

A prolonged orographic precipitation event occurred over the Sierra Nevada in central California on 12–13 February 1986. This well-documented case was investigated via the nonhydrostatic version of the Colorado State University (CSU) Regional Atmospheric Modeling System (RAMS). The two-dimensional, cross-barrier simulations produced flow fields and microphysical structure, which compared well with observations. The feasibility of producing quantitative precipitation forecasts (QPF) with an explicit cloud model was also demonstrated.

The experiments exhibited a profound sensitivity to the input sounding. Initializing with a sounding, which is representative of the upstream environment, was the most critical factor to the success of the simulation. The QPF was also quite sensitive to input graupel density. Decreasing the density of graupel led to increases in the overall precipitation. Sensitivities to other microphysical parameters as well as orography and dynamics were also examined.

1. Introduction

The Sierra Cooperative Pilot Project (SCPP) was initiated in the 1970s to study the natural cloud processes occurring in Sierra Nevada storms. The objectives of the experiment were to identify the conditions when cloud seeding results in an increase or decrease in precipitation, and to monitor the magnitude of those changes (Reynolds and Dennis 1986). The subsequent benefits of SCPP have been a multitude of new insights into the microphysics and dynamics of orographic precipitation. Based on the extensive documentation accumulated during SCPP, a challenge has also been put forth to the modeling community to test their ability to simulate orographic cloud systems and examine the dominant physical controls in these storms.

The structure and organization of cyclonic storms affecting the Sierra Nevada region often resemble the characteristic split-front type (Browning and Monk 1982) evident in the Pacific Northwest (Hobbs 1978) and the United Kingdom (Browning 1985). One contributing factor to the split front is orographic blocking. Blocking results when the cross-barrier flow cools adiabatically as it is forced up the barrier, producing a positive pressure perturbation (Godske et al. 1957; Smith 1979), and a corresponding pressure-gradient force directed upstream from the mountain. This pressure-gradient force decelerates the low-level flow and, in some cases, can even reverse the direction. When a cold front approaches, the cold air advances faster at the higher levels than at lower levels below the mountain crest due to the low-level blocking. This blocking results in cold air being advected over warmer air, commonly leading to a convectively unstable condition (Hobbs et al. 1975; Reynolds and Dennis 1986).

Another symptom of orographic blocking is the mountain parallel wind component, often in the form of a low-level jet (LLJ). This mountain parallel jet was recognized in the polar regions by Schwerdtfeger (1974, 1975). Modeling studies (Parish 1982; Pierrehumbert and Wyman 1985; Smolarkiewicz et al. 1988; Smolarkiewicz and Rotunno 1990) have examined blocked flow in a stratified fluid upstream of ridgelike obstacles. The Sierra Nevada "barrier jet" (Parish 1982) develops when the cross-barrier flow becomes subgeostrophic due to orographic blocking, accelerating the flow toward low pressure in response to the unbalanced pressure gradient in the y direction, and producing a positive v component of the wind. If the flow lasts for several hours the wind field will adjust to the new mass field. This adjustment results in a terrain-locked flow in which the winds in the lowest levels blow nearly parallel to the terrain contours in the form of a barrier jet.

A typical measure of the upstream blocking is expressed by the Froude number

$$\mathrm{Fr} = U/Nh_m,$$

Corresponding author address: Mr. Michael P. Meyers, Colorado State University, Department of Atmospheric Sciences, Fort Collins, CO 80523.

where U is the mean upstream wind speed, N is the Brunt–Väisälä frequency representative over a mountain depth h_m. Moist processes are not considered in this traditional Froude number. The effect of moisture would decrease the stability in the layer weakening the orographic blocking. To account for moisture an alternative approach would be to include the saturated Brunt–Väisälä frequency (Durran and Klemp 1982a) instead of the dry Brunt–Väisälä frequency in the above Froude number. The saturated Brunt–Väisälä frequency (Cotton and Anthes 1989) is then expressed as

$$N_m^2 = \frac{g}{(1 + r_w)}\left[\frac{\gamma_m}{\gamma_d}\left(\frac{d \ln\theta_q}{dz}\right) - \frac{dr_w}{dz}\right].$$

Dramatic alterations of the vertical profile of the Scorer parameter were illustrated by Durran and Klemp (1982b) when a moist Brunt–Väisälä frequency was included in equation.

Diabatic influences can also have an important effect on the blocked flow, as well as the spatial distribution of precipitation. In a stable wintertime orographic case from SCPP, Marwitz (1983) attributed a 3.3-hPa pressure perturbation near the 1-km terrain contour on the barrier to melting. This enhanced blocking can significantly alter the flow field over the barrier by decoupling the flow above the melting layer from the flow below it. With enhanced blocking, the forced orographic ascent is increased, which, in turn, produces more precipitation. Marwitz et al. (1985) applied a two-dimensional version of the Anthes and Warner (1978) hydrostatic model to examine the effects of melting on the flow in the Sierra Nevada region (Cotton and Anthes 1989). In their simulations they calculated a doubling in the intensity of the barrier jet in response to melting. To produce such a dramatic response to melting they concluded that two conditions must be met: first, the flow perpendicular to the barrier must be less than 10 m s^{-1} within the melting layer, so that the adiabatically cooled air is not advected over the barrier; second, the barrier-normal winds above the 0°C isotherm must be 15–20 m s^{-1} to create an ascent rate large enough to produce precipitation rates of 3–4 mm h^{-1}. These melting effects are greatest when the maximum vertical shear of the barrier-normal wind is near the 0°C isotherm.

Other factors that may govern the amount and type of precipitation in orographic wintertime storms include the distribution of liquid water and the seeder–feeder mechanism. The distribution of supercooled liquid water (SLW) is a determining factor on the amount and type of precipitation, which falls in wintertime orographic clouds. Reynolds and Dennis (1986) note that the bulk of the SLW was confined below the −10°C level. Heggli (1986) suggests a bimodal vertical distribution of liquid water. A low-level maximum occurs between −2° and −4°C and another maximum between −10° and −12°C. Marwitz (1987) found a highly concentrated layer of ice crystals (many of which were needles) near the −5°C level, several orders of magnitude greater than the ice nuclei concentrations described by Fletcher (1962), suggesting that a secondary multiplication process such as that described by Hallett and Mossop (1974) was occurring. The other process that may affect the distribution of orographic precipitation is the seeder–feeder mechanism. Bergeron (1949, 1965) hypothesized that cloud liquid water produced by the orographic lift (feeder cloud) may be depleted by precipitation falling from upper-level clouds formed by large-scale ascent (seeder cloud). The seeder cloud precipitation may originate either by collision/coalescence or, as in the case of Sierra wintertime storms, by ice-phase precipitation. Bergeron (1949) pointed out that certain precipitation patterns were linked to surface topography of very limited height. He later explained that small terrain features of the order of 50 m in height may cause the formation of low-level feeder clouds, which can increase precipitation amounts 25%–50% (Bergeron 1965). More recent studies (Rauber 1981; Cotton et al. 1986) suggest that smaller hills upstream of major mountain barriers alter the ice–water budgets of clouds forming over the main barriers. Rauber (1981) also calculated that due to the low terminal velocity of pristine ice crystals, the precipitation from upper-level seeder clouds would have to start settling 100 km upstream in order to affect the barrier precipitation. In northern California, the seeder–feeder mechanism is further complicated by the presence of the Coast Range located 120 km upstream of the Sierra Nevada. Additional research is needed to clarify the role of upstream topography on cloud and precipitation processes over the primary barrier.

The purpose of this paper is to apply the Colorado State University (CSU) Regional Atmospheric Modeling System (RAMS) to the SCPP case study day on 12 February 1986. This case represents an excellent opportunity to evaluate the ability of the model to predict the precipitation distribution and the kinematic and microphysical structure of a quasi-steady orographic cloud system over the Sierra Nevada region of California. The detailed observations described by Rauber (1992) allow a quantitative verification of the model while the increased resolution available in the model can enhance our understanding of the physical processes responsible for the observed precipitation distribution.

2. Case study

The cloud system that affected central California on 12 February 1986 originated over the south-central Pacific and was characterized by warmer than normal temperatures. The microphysical and kinematic struc-

tures are described in detail by Rauber (1992), hereafter referred to as R92. The focus of this numerical examination is the time period after the passage of a weak trough evident at 1500 UTC (see R92, Fig. 3), where a layer of potential instability existed at the top of the lower moist level. The cloud structure at this time was rapidly deepening and building westward across the Central Valley (see R92, Figs. 7–11). Precipitation was evident over the length of the barrier, with maximum amounts observed 40 km upwind of the crestline (see R92, Fig. 12). A conceptual model of the precipitation processes observed in this case study is described in R92 (Fig. 18). This conceptual model emphasizes two intersection zones: first, where the cloud droplets rising through cloud base above the Sierra Nevada barrier intersects with the dendritic zone descending from the upper cloud leading to secondary ice-crystal production due to rime splintering; and, second, where these crystals produced by secondary ice production interacted with dendritic aggregates near barrier crest. The precipitation maximum observed in this case study corresponds to the fallout locations of the first intersection zone. The kinematic structure was highlighted by a barrier jet of nearly 25 m s^{-1} (see R92, Fig. 4). Froude number calculations for the case based on the initial sounding were 0.5, which is indicative of blocked flow. Using the modified Froude number that includes the effects of moisture increased the Froude number to 0.7, still representative of blocked flow but weaker than with the dry Froude number calculations.

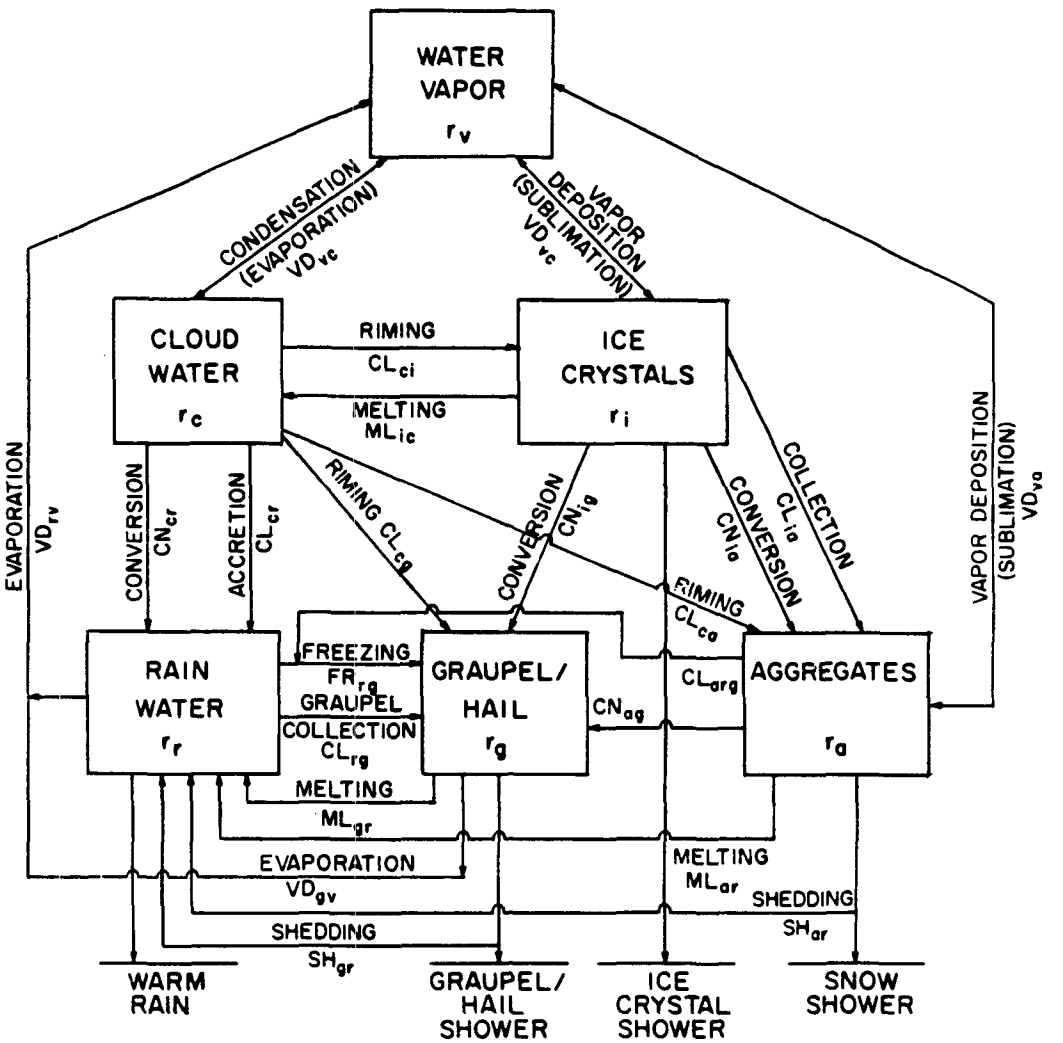

FIG. 1. Flow diagram describing microphysical processes considered in model. The source and sink terms are defined as CN for conversion, ML for melting, FR for freezing, CL for collection, VD for vapor deposition or evaporation, and SH for liquid water shedding. Each term includes a double subscript, where the first subscript is the water phase being depleted and the second subscript is the water phase that is growing. The subscripts, *v*, *c*, *r*, *i*, *g*, and *a* refer to vapor, cloud, rain, pristine ice crystal, graupel, and aggregate water species, respectively.

3. Experimental design

The numerical model used in this study is a version of the CSU RAMS cloud model (Tripoli and Cotton 1982; Cotton et al. 1982, 1986). The model is based on the nonhydrostatic, fully compressible momentum equations, a thermodynamic energy equation, and equations for liquid- and ice-phase precipitation processes. The predicted variables include the three velocity components, the Exner function π, the ice–liquid water potential temperature θ_{il}, pristine ice-crystal concentrations, and mixing ratio of total water, rainwater, pristine ice crystals, graupel particles, and aggregates (Cotton et al. 1986). Potential temperature, temperature, cloud-droplet mixing ratio, water vapor mixing ratio, and pressure are calculated diagnostically (Tripoli and Cotton 1982). A flow diagram of the microphysical processes used in the model is given in Fig. 1. A comprehensive overview of the microphysics model is given in Flatau et al. (1989). Horizontal and vertical turbulence are parameterized using an eddy viscosity closure scheme, as described by Tripoli and Cotton (1982). The equations are integrated numerically by a time-splitting procedure for a nonhydrostatic, compressible system (Tripoli and Cotton 1982) with a large time step of 5 s and a small time step of 2.5 s. Since mountain waves play an important role in determining the flow fields in orographic clouds, the Klemp and Durran (1983) radiative-type top boundary condition was used. The lateral boundary conditions employed were the Klemp and Wilhelmson (1978) radiative type together with a mesoscale compensation region outside the simulation domain (Tripoli and Cotton 1982). A terrain-following sigma-z vertical coordinate system is used following Gal-Chen and Sommerville (1975a,b).

In this study, two-dimensional simulations will facilitate sensitivity experiments to be performed due to the computational costs. The results of three-dimensional simulations will be described in a subsequent paper. A diagram of the domain with the topography is shown in Fig. 2. Since the Sierra Nevada is oriented approximately north-northwest to south-southeast, the horizontal plane was assumed to be perpendicular to the barrier, thus, maximizing the topographical gradient of the barrier resolved by the model. The model domain is 450 km long and extends 14.5 km in the vertical. The horizontal grid resolution is 1.5 km, which should sufficiently resolve small-scale precipitation processes important for mesoscale precipitation forecasting. The Coast Range was also included to investigate its upstream effect on airflow over the Sierra Nevada barrier. The vertical grid resolution is 0.25 km from the surface to the barrier crest and stretched to a constant vertical resolution of 0.5 km above 10 km. The increased resolution in the lowest layers allows a

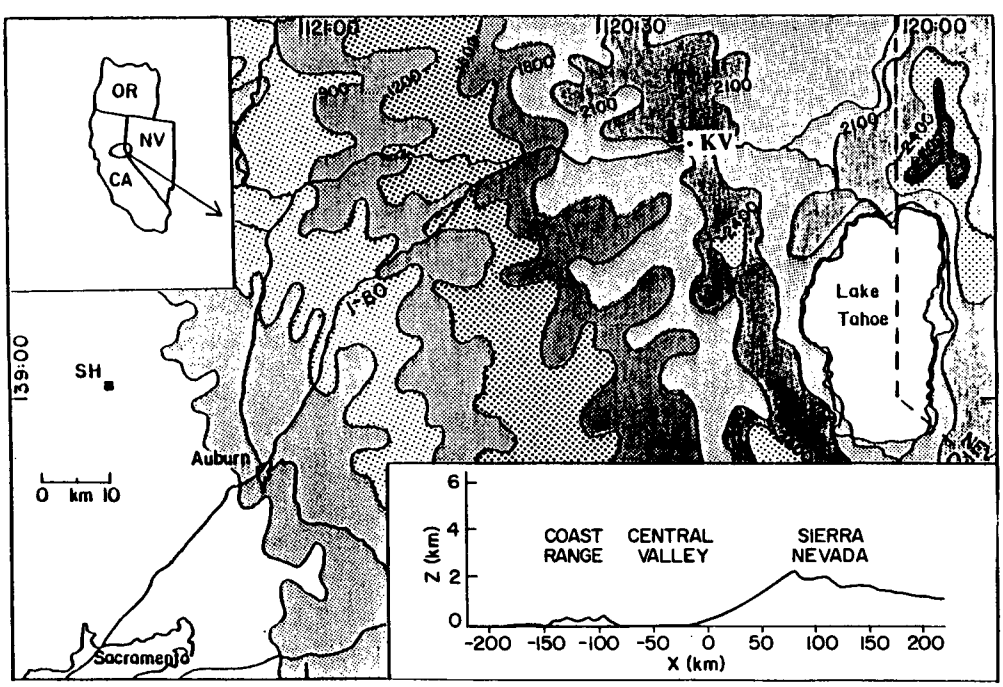

FIG. 2. Topographic map of the SCPP area (adapted from Rauber 1992), with a state map shown in the inset in the upper left, and horizontal slice of topography used in simulations shown in the inset in the lower right. Sheridan soundings were launched at SH.

more realistic depiction of the microphysical and thermodynamical structure of the cloud system.

a. Initialization

One major drawback of modeling in the Sierra Nevada region is that the wind profile is strongly influenced by the barrier in the lowest levels making it nearly impossible to get a representative wind profile in this region. The sounding used to initialize the model in the simulations are a hybrid sounding with the thermodynamic sounding from Sheridan, California, and the geostrophic winds inferred from National Meteorological Center (NMC) synoptic charts. The thermodynamic sounding chosen from Sheridan was the sounding at 1500 UTC 12 February 1986 (Fig. 3a) due to its proximity to the most intensive aircraft and radar observations of the storm. The thermodynamic structure exhibited a deep, moist layer that extended up to the 0°C level with drying occurring above the layer up to the −10°C level. A potentially unstable layer exists from the top of the lower moist level (2 km) to 4 km. The Sheridan winds were not used because these winds were determined to be not representative of the flow entering the western boundary of the domain. Preliminary tests (Meyers 1989) compared the model response to the geostrophic winds inferred from NMC synoptic charts at 1200 UTC (sounding I) to the actual Sheridan, California, sounding winds at 1500 UTC (sounding II) as the initial wind profile (Fig. 3b). The main differences between the wind profiles were below barrier crest where sounding I showed uniformly strong cross-barrier winds, while sounding II showed the station in blocked, light winds near the surface, and a barrier jet near 1 km MSL. A 100-gridpoint domain

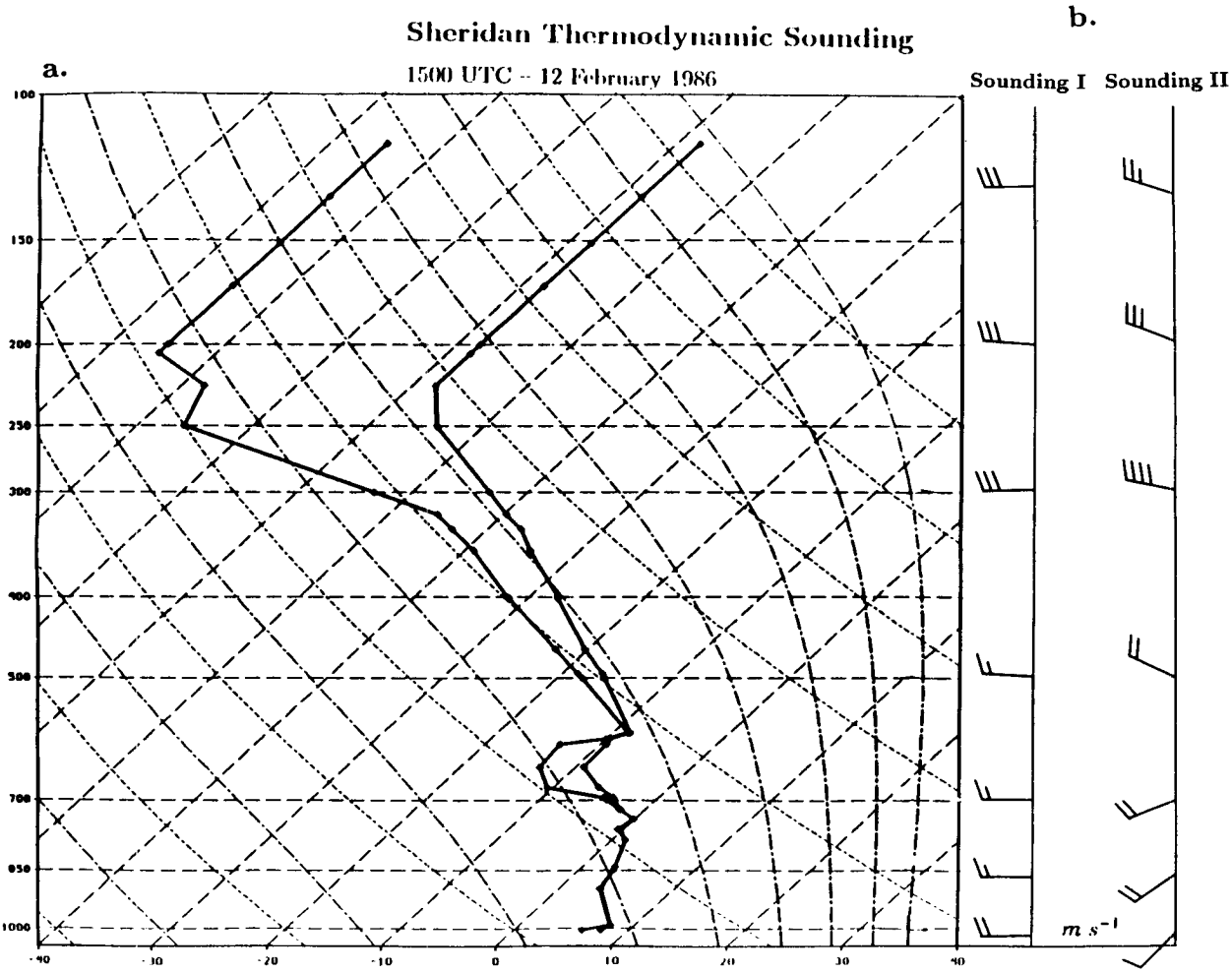

FIG. 3. (a) The 1500 UTC 12 February 1986 Sheridan thermodynamic sounding. Temperatures and dewpoint are displayed. (b) Geostrophic winds inferred from NMC synoptic maps at 1200 UTC (sounding I), and the actual Sheridan sounding winds at 1500 UTC (sounding II). Winds are in meters per second.

with coarser horizontal resolution (3 km), no microphysics, and simple topography was used. The time-dependent variables in this study were initialized with a horizontally homogeneous interpolation of the sounding. These tests showed that the simulation initialized with sounding I produced a more dynamically consistent flow, which compared more favorably with the observations than the simulation initialized with sounding II. Another advantage of sounding I was that features such as the barrier jet were not initialized into the sounding, allowing the flow to evolve and the mass and momentum fields to balance on their own. Therefore, sounding I was used in the control run and sounding II was used to examine the sensitivity of the model to the initial wind profile.

Since the numerical study contains flow over a mountain barrier, the flow field must be dynamically initialized, adding the winds incrementally during the first 30 min, as described by Tripoli and Cotton (1989). The model is then allowed to adjust to these winds for a 2.5-h period during which time all microphysical tendencies are deactivated. Cloud water, however, is allowed to form when saturation occurred. At 3.0 h the full microphysics module is activated and the simulation is run out to 6.0 h. The Coriolis parameter is activated for all but one of the simulations.

b. Numerical experiments

A short description of all the simulations is given in Table 1. The approach in this study will be to set up a control experiment that simulates the observed kinematic, microphysical, and thermodynamic structure of the atmosphere. The simulated precipitation distribution should compare well with observations if these constraints are met. Once a control experiment is established, sensitivity experiments will be compared to the control experiment to reveal the dominant physical controls on orographic cloud and precipitation processes. First, a dry run will be presented to examine the role of latent heating on the kinematic structure of the orographic storm system. The diabatic influences of melting on the dynamic and thermodynamic structure will also be investigated. An experiment to evaluate the sensitivity of the model to the initial wind profile using sounding II (Fig. 3b) will be conducted. An investigation turning off the Coriolis parameter will be conducted to evaluate the importance of the barrier jet on QPF in two-dimensional simulations. The effects of the upstream Coast Range on the precipitation distribution, and specifically its impact on seeder–feeder processes will be examined. Finally, the sensitivity of orographic wintertime storms to the model microphysics will be investigated.

TABLE 1. Simulated experiments with short description.

Experiment I:	Control run initialized with sounding I; full microphysics 3–6 h
Sensitivity I:	Dry run, same as control run, except no microphysics and condensation
Sensitivity II:	Same as control run, except with no melting
Sensitivity III:	Initialized with sounding II; full microphysics 3–6 h
Sensitivity IV:	Same as control run, except with Coriolis turned off
Sensitivity V:	Same as control run, except with no Coast Range
Sensitivity VI:	Same as control run, except no graupel
Sensitivity VII:	Same as control run, except graupel density = 0.9 g cm^{-3} instead of 0.45 g cm^{-3}
Sensitivity VIII:	Same as control run, except graupel density = 0.1 g cm^{-3} instead of 0.45 g cm^{-3}
Sensitivity IX:	Same as control run, except no secondary ice production
Sensitivity X:	Same as control run, except CCN is 5 cm^{-3} instead of 60 cm^{-3}
Sensitivity XI:	Same as control run, except CCN is 200 cm^{-3} instead of 60 cm^{-3}

4. Numerical results

Subsequent figures shown in this paper are at 6 h of simulation unless otherwise noted. By 6 h the geostrophic adjustment process in the model was not complete. The lack of complete geostrophic adjustment mainly affects the strength of the barrier jet, which in previous simulations was found to increase in speed beyond 6 h (Meyers 1989; Parish 1982). The model approaches a quasi-steady solution though transient resolvable meso-γ (Orlanski 1975) features still exist. Subsequent figures do not cover the entire model domain to allow a more focused inspection of the region of interest from the Coast Range to the Sierra Nevada crest.

a. Control experiment

1) KINEMATIC STRUCTURE

The simulated wind and pressure fields of the control experiment are shown in Fig. 4. The u component of the wind (Fig. 4a) decelerates to less than 2 m s^{-1} near the surface at the base of Sierra Nevada barrier. The gradient of the u-component wind increases as the barrier crest is approached with winds close to 18 m s^{-1} at the top of the crest. The observed u-component winds showed weak winds near the base of the barrier with a u-component wind of 20 m s^{-1} near the top of the barrier. The v-component field (Fig. 4b) shows an elongated jet core near the base of the barrier with its location comparing well with SCPP observations (see R92, Fig. 4). The magnitude of the barrier jet core (9 m s^{-1}) is less than half of what was observed, but as already noted, 6 h of simulation is not nearly enough time to allow full geostrophic adjustment to take place. Another explanation for the weaker barrier jet is due

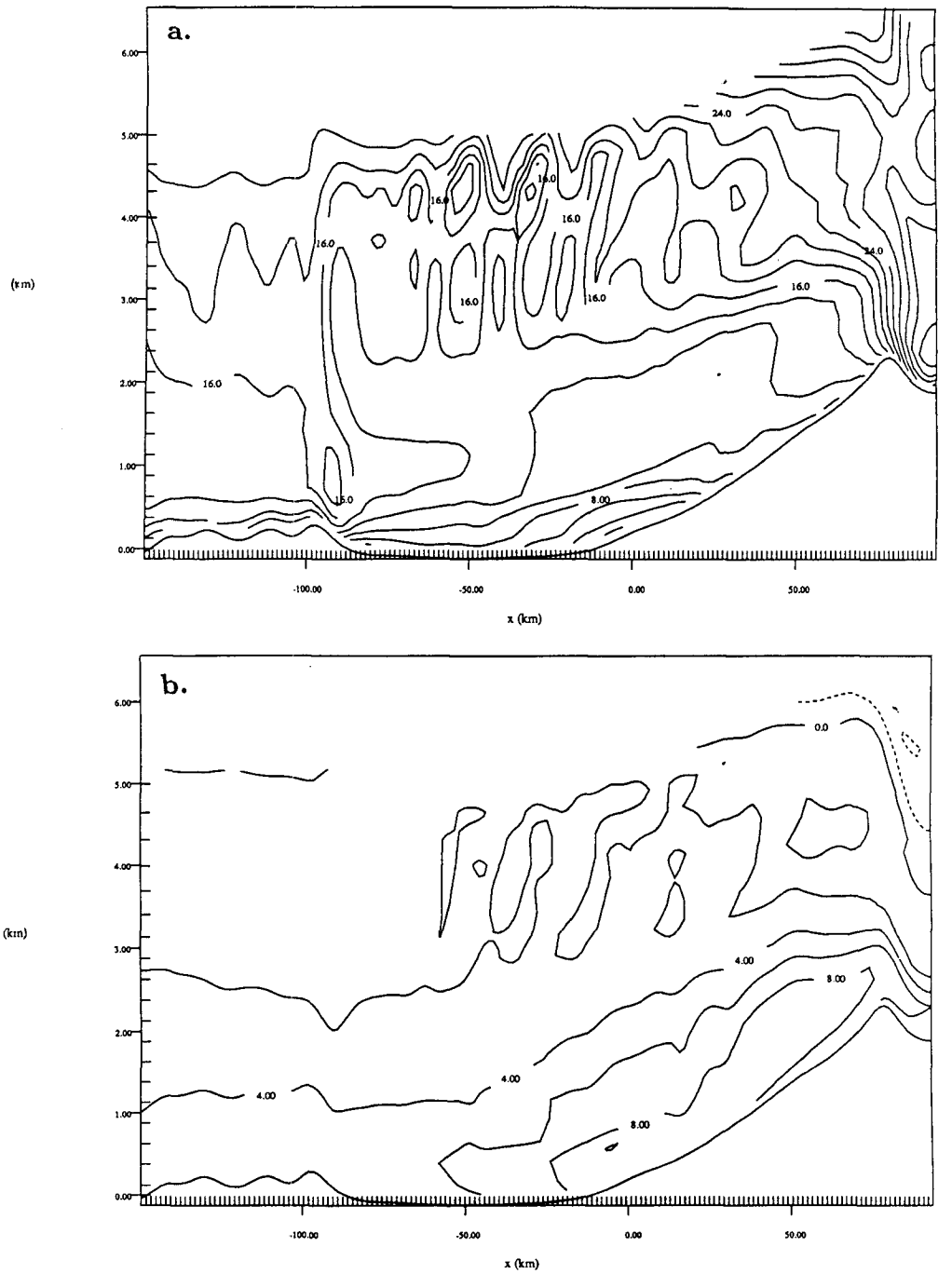

FIG. 4. Simulated wind and pressure fields for the control run (a) u component of the wind, the contour interval is 2.0 m s^{-1}; (b) v component of the wind, the contour interval is 2.0 m s^{-1}; (c) pressure perturbation field, the contour interval is 0.4 mb; (d) w component of the wind, the contour interval 0.2 m s^{-1}. The w component of the wind is windowed in more than the other fields for clarity. Solid lines are positive and dashed lines are negative. All fields shown at 6 h of simulation time. The abscissa and ordinate are in kilometers.

to the thermodynamic structure of the initial profile. The initial profile was taken from a sounding well into the storm history, which included a potentially unstable layer. Orographic blocking was still evident in these simulated fields, as indicated by the modified Froude number of 0.7. Moist processes also destabilized the environment enough to become potentially unstable. This instability enabled the flow to be lifted over the

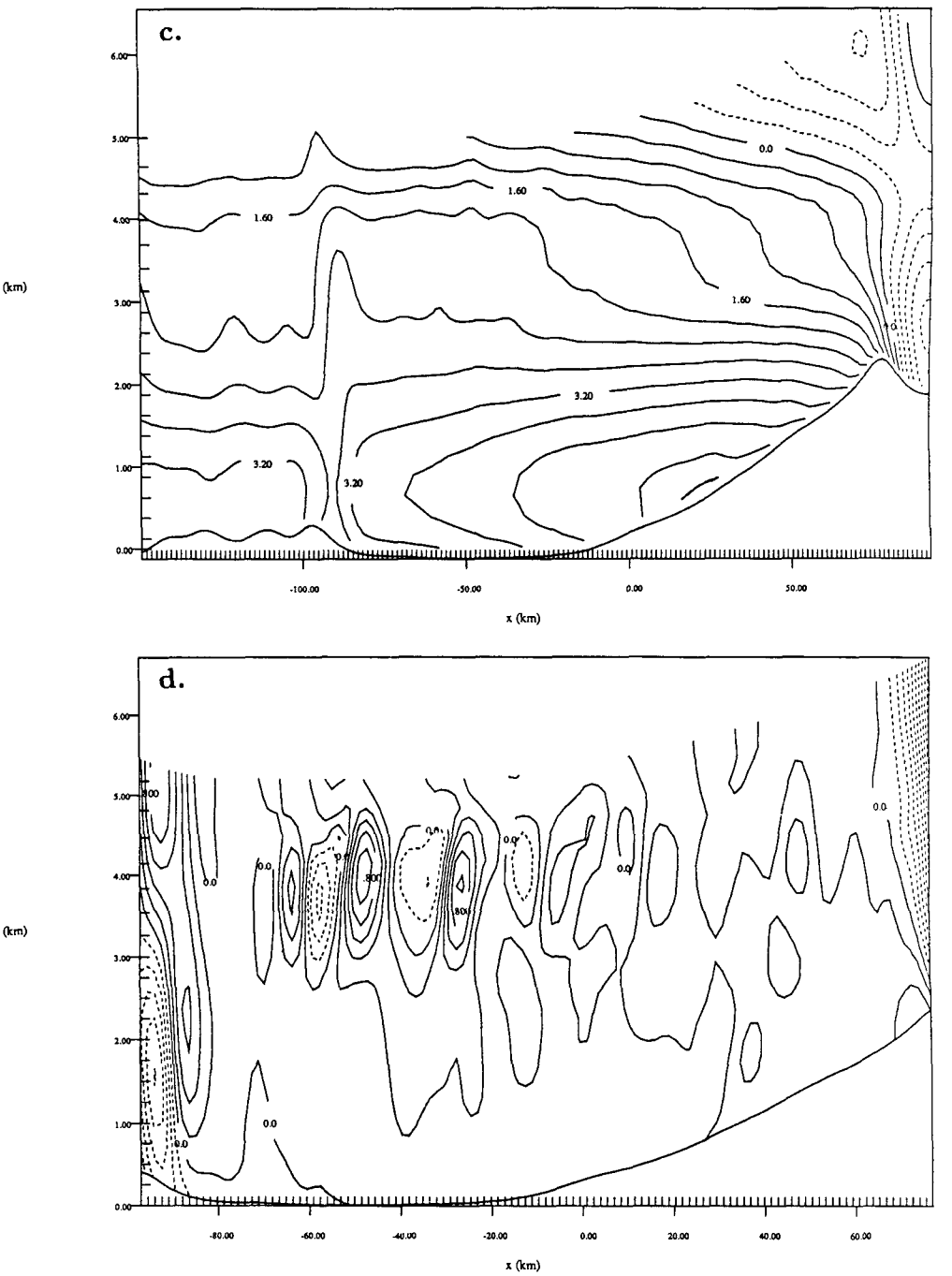

FIG. 4. (*Continued*)

Sierra barrier, which lessened the orographic blocking resulting in a weaker barrier jet.

Positive pressure perturbations (Fig. 4c) extend over the barrier with peak values of 4.8 hPa centered on the barrier. This blocked flow should enhance upward motion over the lower portion of the barrier, concentrating peak precipitation amounts just downstream from this location. The w-component field (Fig. 4d) indeed shows enhanced upward motion just above the strongest pressure perturbations upwind of the barrier crest between 2 and 4 km MSL. Another interesting feature seen in the vertical-motion field is a cellular-type structure located upstream of the Sierra Nevada crest. This feature is forced by westerly flow impinging

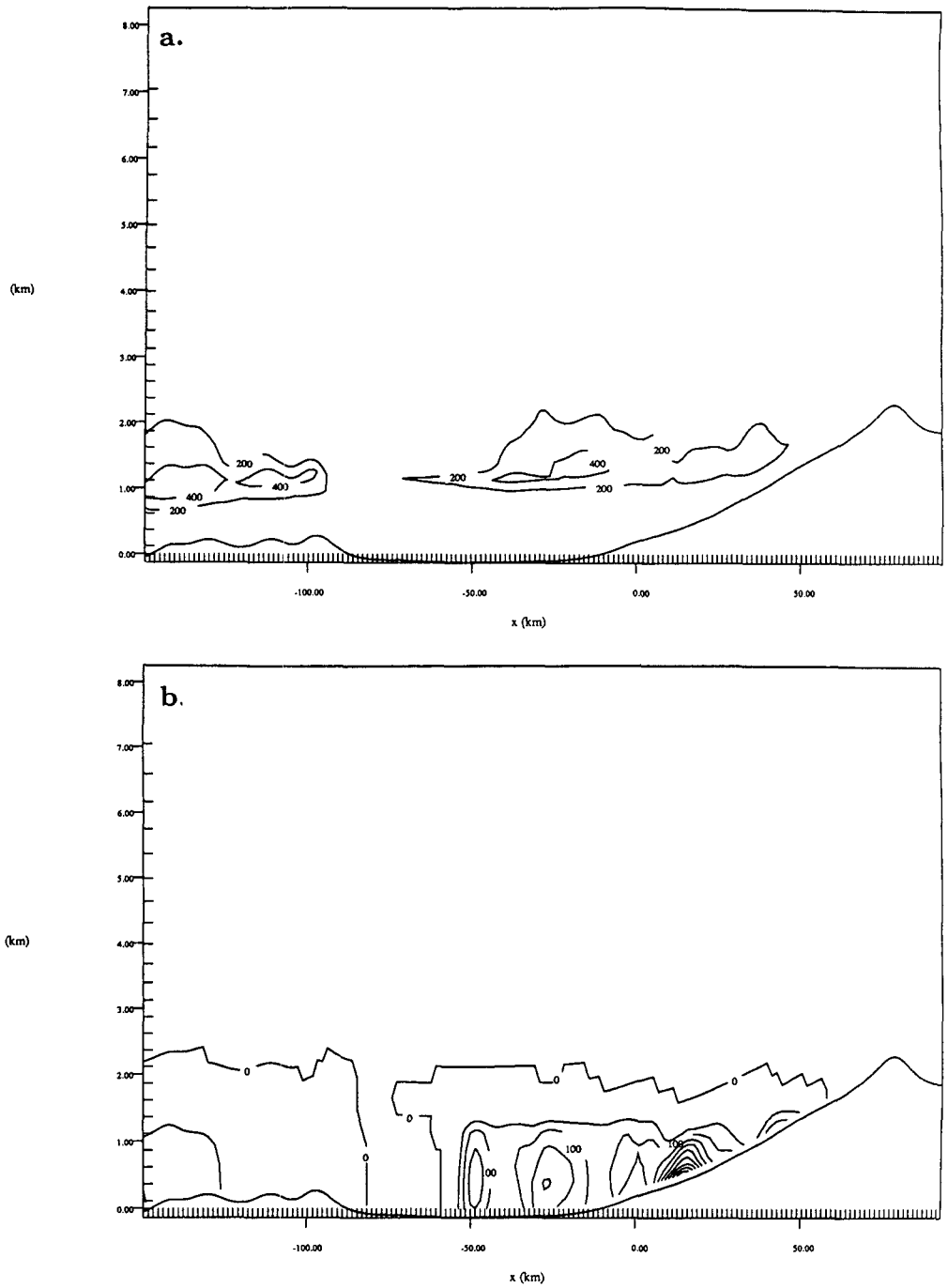

FIG. 5. Simulated microphysical fields for the control run of (a) cloud water, the contour interval is 0.2 g kg^{-1} and the maximum value is 0.4 g kg^{-1}; (b) rainwater, the contour interval is 0.05 g kg^{-1} and the maximum value is 0.45 g kg^{-1}; (c) pristine ice crystals, the contour interval is 0.2 g kg^{-1} and the maximum value is 1.0 g kg^{-1}; (d) aggregates, the contour interval is 0.2 g kg^{-1} and the maximum value is 1.0 g kg^{-1}; (e) graupel, the contour interval is 0.1 g kg^{-1} and the maximum value is 0.5 g kg^{-1}. The contour labels are 10^3 g kg^{-1}. All figures shown are at 6 h of simulation time. The abscissa and ordinate are in kilometers.

on the blocked stable air, which extended westward across the valley. This blocked air becomes an "equivalent" barrier forcing the ambient flow upward through a deeper layer. With a convectively unstable layer present between 2 and 4 km MSL, as mentioned earlier, cloud bands were initiated analogous to those described in Smolarkiewicz et al. (1988). These bands propagate downstream with the flow and impact precipitation

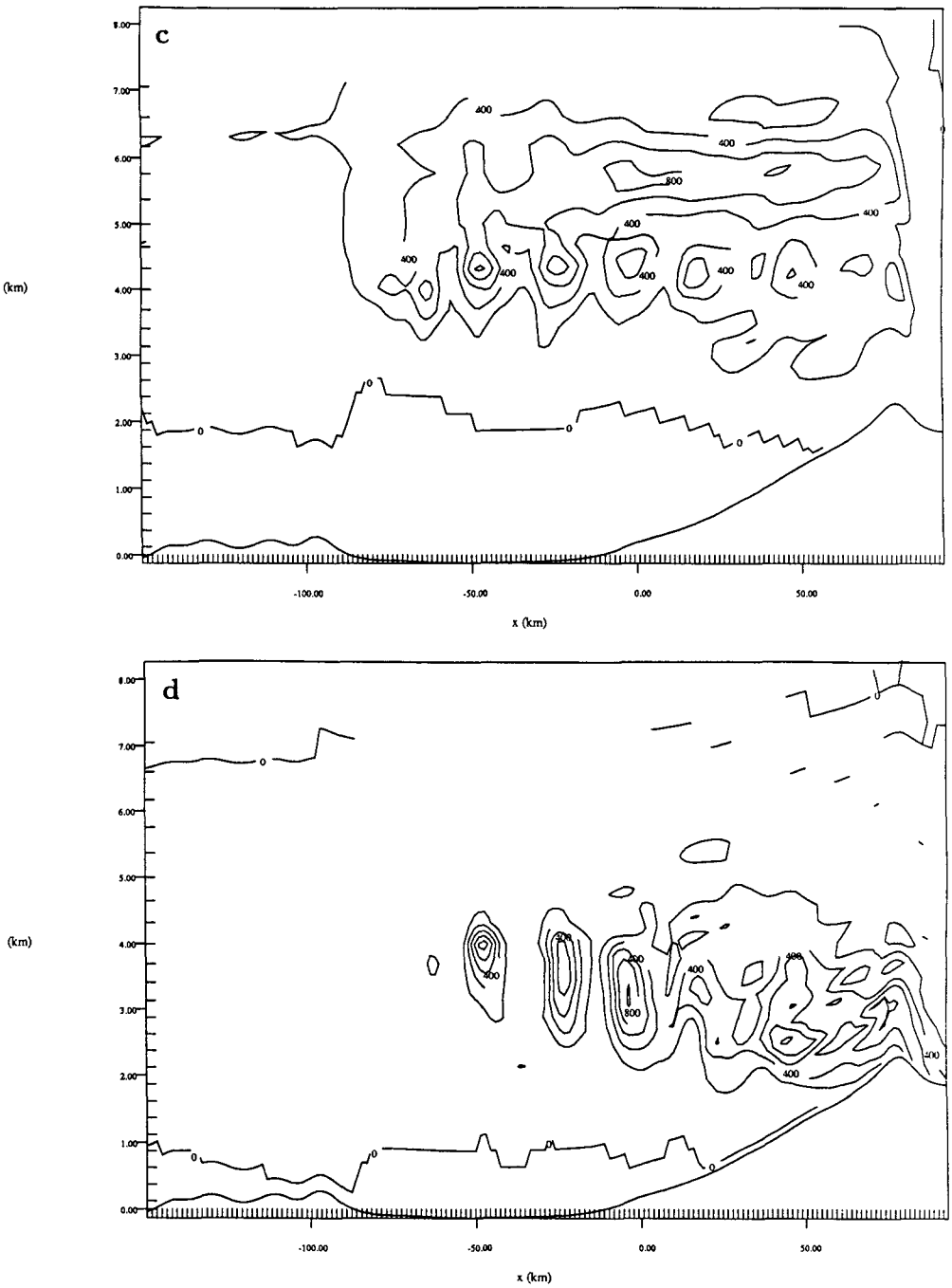

FIG. 5. (*Continued*)

processes in the simulation. An additional examination of the cells will be conducted in the dry run where latent heat influences are excluded.

2) MICROPHYSICAL STRUCTURE

The simulated microphysical fields showed extensive temporal evolution in response to the transient convective bands that propagated downstream across the Central Valley. These transient features illustrate that we are not dealing with a classic steady flow over a stably stratified mountain barrier. Therefore, the microphysical fields at 6 h of simulation time are a "snapshot" picture and not necessarily representative of the ensemble-averaged fields over the whole period.

The simulated cloud-water mixing ratio shown in

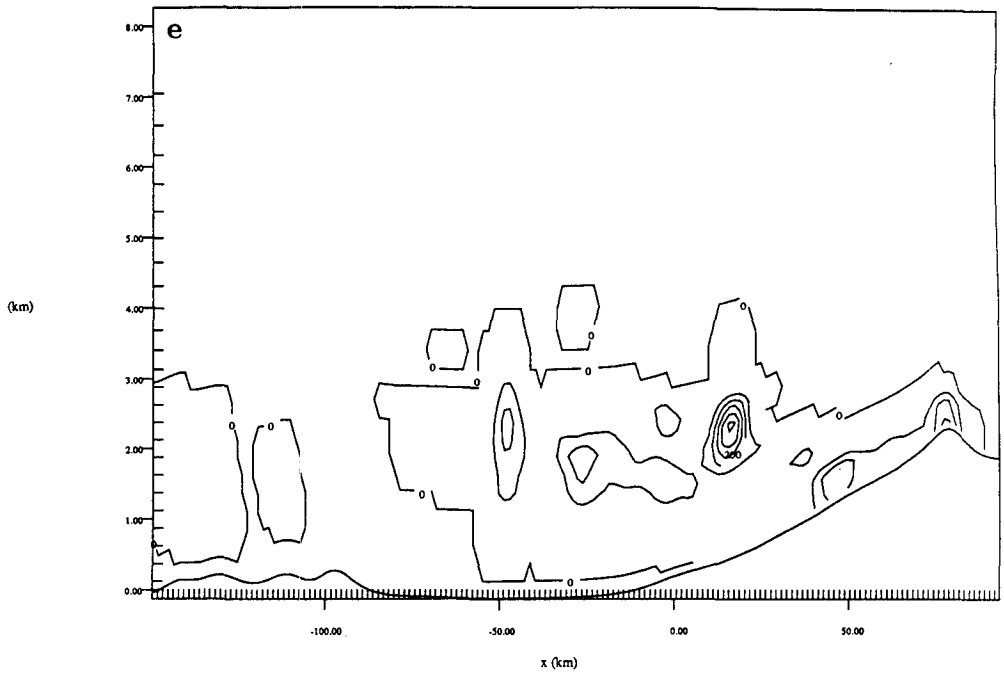

FIG. 5. (*Continued*)

Fig. 5a displays a break in the cloud water just to the lee of the Coast Range. The break is a result of drying occurring due to strong subsidence in the downward branch of the mountain wave to the lee of the Coast Range. The rain mixing ratio field (Fig. 5b) extends up most of the Sierra Nevada barrier with one well-defined peak over the lower half of the barrier. Quantities of rain decrease westward across the valley with light amounts over the Coast Range. The pristine ice-crystal mixing ratio field (Fig. 5c) compares well with observations (see R92, Fig. 18): the cloud top at 7 km MSL extends upstream from the Sierra crest to the Coast Range. Evident to the lee of the crest is a sharp cutoff of the pristine ice crystal mass field due to the strong downward motion in the lee wave. Cellular peaks in the pristine ice-crystal mass field are well correlated with the upward vertical velocities shown in Fig. 4b. The simulated aggregate mixing ratio field (Fig. 5d) shows aggregates reaching the ground near and to the lee of the crest, which also compares well with the observations. The graupel mixing ratio field (Fig. 5e) again exhibits a cellular structure similar to the other microphysical fields, but with one distinct peak near 2.0 km MSL above the middle of the barrier.

3) PRECIPITATION DISTRIBUTION

The simulated precipitation distribution, shown in Fig. 6a, shows the heaviest amounts occurring on the middle half of the barrier where the observed maximum was located (see R92, Fig. 12). Simulated maximum precipitation amounts were nearly 20% greater than the observations. Precipitation amounts decrease sharply to the lee of the barrier crest. To the west of the Sierra barrier, over the Central Valley, amounts decrease steadily with a minimum to the lee of the Coast Range, but a secondary peak is evident over the Coast Range. Radar scans (see R92, Fig. 6) indicated that precipitation was occurring over the Central Valley.

One advantage of explicit simulation of microphysics is that the contributions of the various precipitation types to surface precipitation can be examined. Figure 6b shows the rain, aggregate, and graupel surface precipitation amounts. The rain distribution displays the highest totals on the lower half of the Sierra barrier. There is also a secondary peak on the windward side of the Coast Range. The rain distribution shows a sharp cutoff on the upper half of the barrier where the ice-phase precipitation was more widespread. The graupel distribution is dominant over the upper half of the barrier and the aggregate precipitation is found near the barrier crest. The locations compare well with the locations of precipitation type shown in the conceptual model (see R92, Fig. 18). The predominance of graupel and rain due to melted graupel over the middle of the barrier indicates that heavy riming was occurring in the simulation. This location is just upstream of the first intersection region described earlier.

b. The dry run

To determine the latent heat impact and microphysical influences on the kinematic structure obtained

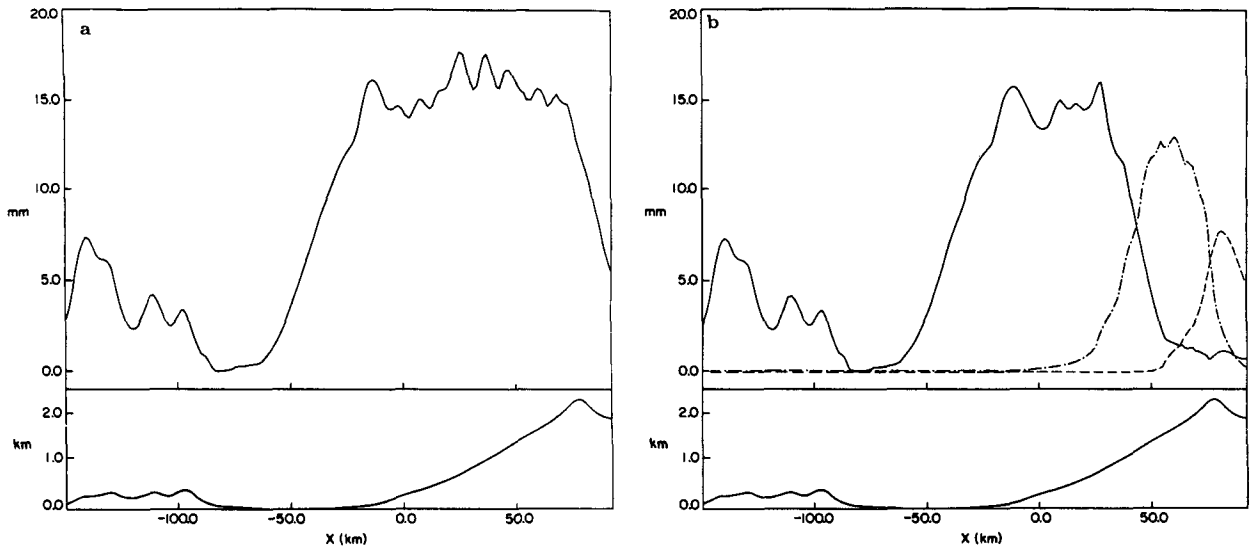

FIG. 6. (a) Precipitation distribution for the control run, for 3-h period with topography distribution scaled below. (b) Precipitation distribution of (i) rain (solid lines); (ii) aggregates (dashed lines); (iii) graupel (dash–dot) for 3-h period with topography scaled below. The abscissa is in kilometers and the ordinate is total precipitation amount in millimeters.

in the control run, the model was rerun with all diabatic influences turned off. Water vapor and its virtual temperature effects were included. In some respects, this simulation resembles the modeling work done by Parish (1982). In both cases diabatic influences were not considered. Parish, however, used an idealized initial wind profile and his topography did not include the Coast Range.

The results shown in Fig. 7 indicate a substantial sensitivity to latent heat effects. The u-component field (Fig. 7a) shows the strongest horizontal shear over the upper half of the barrier with weakest winds near the base of the barrier. A stronger upwind component was evident over the base of the barrier in the dry run than in the control run. The v component (Fig. 7b) shows a dramatic elongated barrier jet with strongest values of 17 m s^{-1} situated above the middle half of the barrier. The pressure perturbation field (Fig. 7c) exhibits a strong pressure excess located near the base of the Sierra Nevada barrier. Peak values are 8.8 hPa near the base of the barrier, nearly twice as large as the control run. Peak positive pressure perturbations were much larger in the dry run than in the control run due to the deactivation of diabatic influences and greater adiabatic cooling. The Froude number for the dry case was calculated to be 0.5, which is indicative of strong orographic blocking. The influence of moist processes, especially due to potential instability, was absent in this sensitivity experiment resulting in more orographic blocking than was simulated in the control run. The barrier jet was much stronger than the control run, which compared more favorably with observations. With stronger orographic blocking evident in the dry run, the acceleration toward lower pressure to the north was greater to compensate for the unbalanced pressure gradient in the y direction, producing a significant barrier jet. With time, Coriolis forcing in the x direction would accelerate the u-component field back toward geostrophy (Pierrehumbert and Wyman 1985), which accounts for stronger u-component winds over the barrier in the dry run. The vertical velocity field (Fig. 7d) exhibits strong positive motions near the peak of the barrier with values of 0.8 m s^{-1}. The vertical motions upstream of the barrier are weak compared to the control run. Absent from this dry experiment is the upstream wave structure, which was evident in the control run. Although the mechanism responsible for the upward motion in the control run was the orographic blocking, the trigger that enabled the cells to develop was the layer of potential instability between 2 and 4 km MSL. With latent heat influences absent in the dry run, wet potential instability was not realized.

These results are, for the most part, consistent with Parish's findings. The horizontal winds are very similar, but the barrier jet in Fig. 7b is slightly weaker and farther up the barrier. These differences can possibly be explained by differences in the initial wind profile, thermodynamic stability, and topographic representation.

c. *Sensitivity to diabatic influences of melting*

The importance of melting to orographic precipitation has been discussed by Marwitz (1983). He attributed a 3.3 hPa excess of pressure along the barrier to the diabatic influences of melting. A doubling of the barrier jet was also calculated in modeling work performed by Marwitz et al. (1985) under certain con-

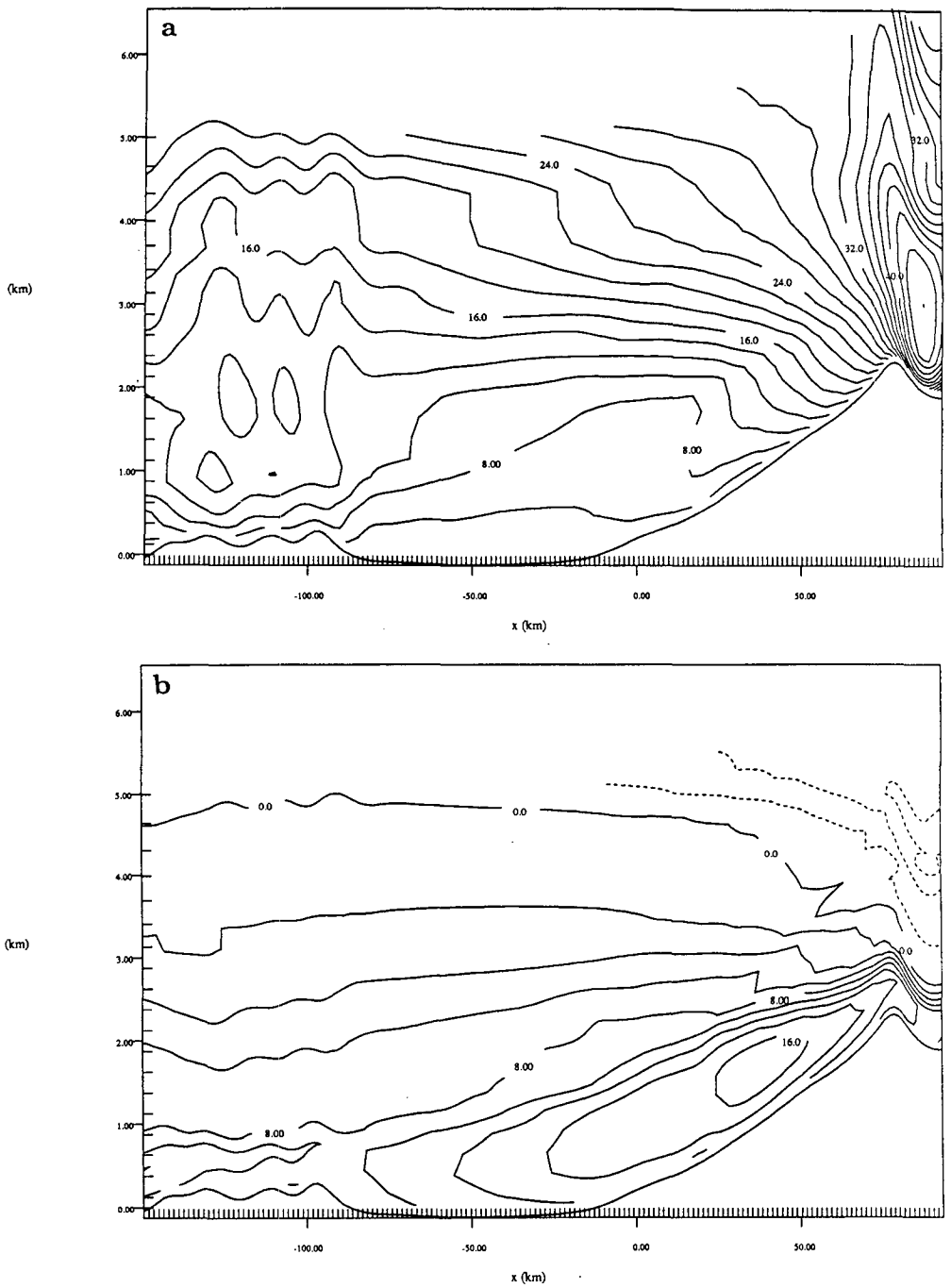

FIG. 7. Simulated wind and pressure fields for the dry run of (a) u component of the wind, the contour interval is 2.0 m s^{-1}; (b) v component of the wind, the contour interval is 2.0 m s^{-1}; (c) pressure perturbation field, the contour interval is 0.8 mb; (d) w component of the wind, the contour interval 0.2 m s^{-1}. The w component of the wind is windowed in more than the other fields for clarity. Solid lines are positive and dashed lines are negative. All fields shown at 6 h of simulation time. The abscissa and ordinate are in kilometers.

ditions. To examine the effect of melting, the model has been altered in this experiment so that no conversion from the ice phase to the liquid phase could occur, eliminating the diabatic response of melting. Unlike the previous sensitivity experiment, sublimation and evaporation processes remained in the model.

The horizontal wind fields (Figs. 8a and 8b) are quite similar to the wind fields seen in the control run. The

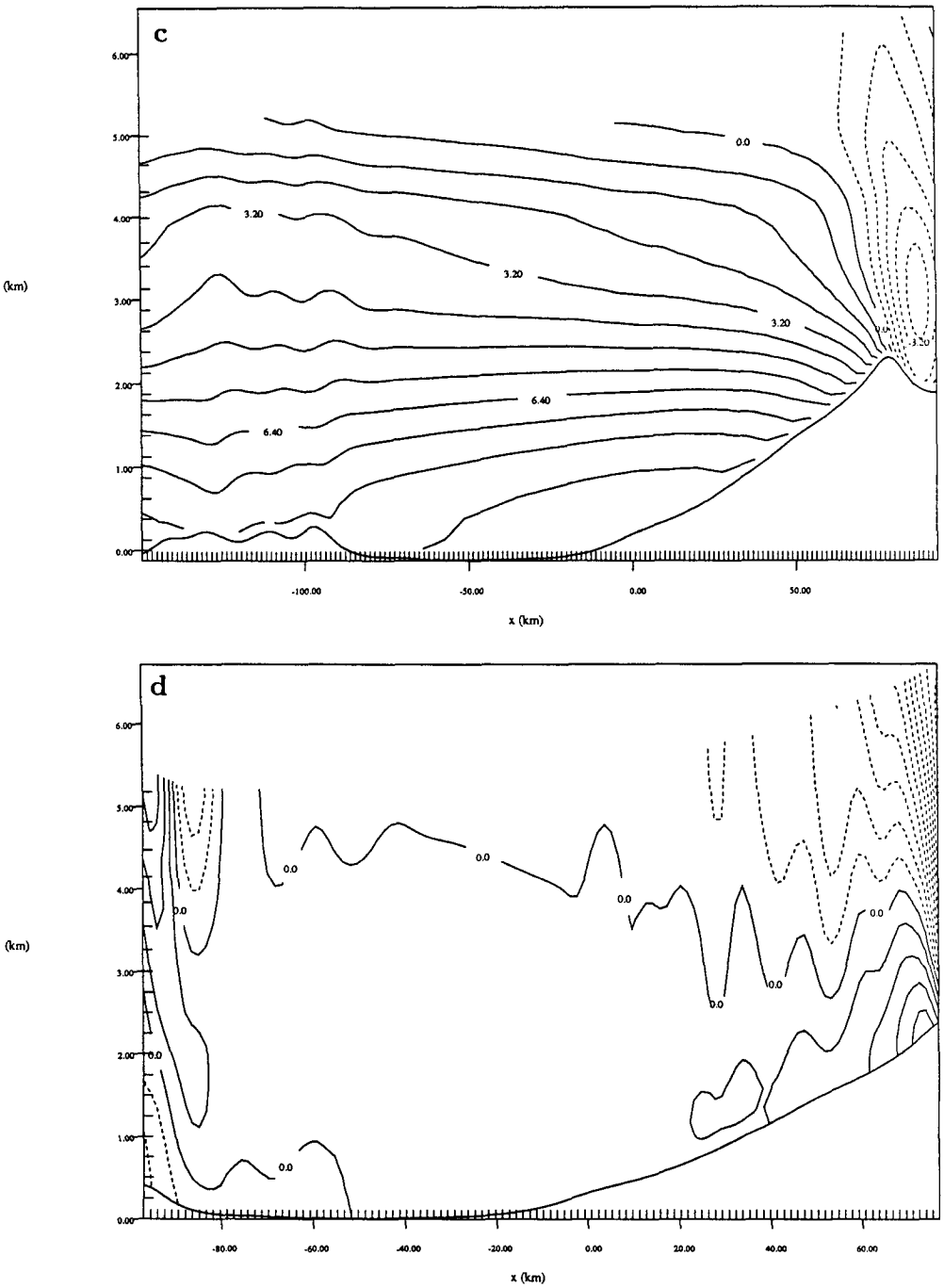

FIG. 7. (*Continued*)

barrier jet showed no appreciable change with the diabatic influences of melting turned off. Marwitz et al. (1985) noted two conditions must be met for a significant response to melting, such as strengthening the barrier jet, to be recognized. In the 12 February 1986 case, the flow in the melting layer is between 10 and 12 m s^{-1}, which is slightly greater than the threshold value mentioned earlier. The second condition that precipitation rates be at least 3–4 mm h^{-1} was observed in this case. Marwitz et al. (1985) also note that the melting effects are greatest when the maximum shear of the barrier-normal winds are near the 0°C isotherm. In our case, however, the greatest shear of the barrier-normal wind is over the lower half of the barrier, below

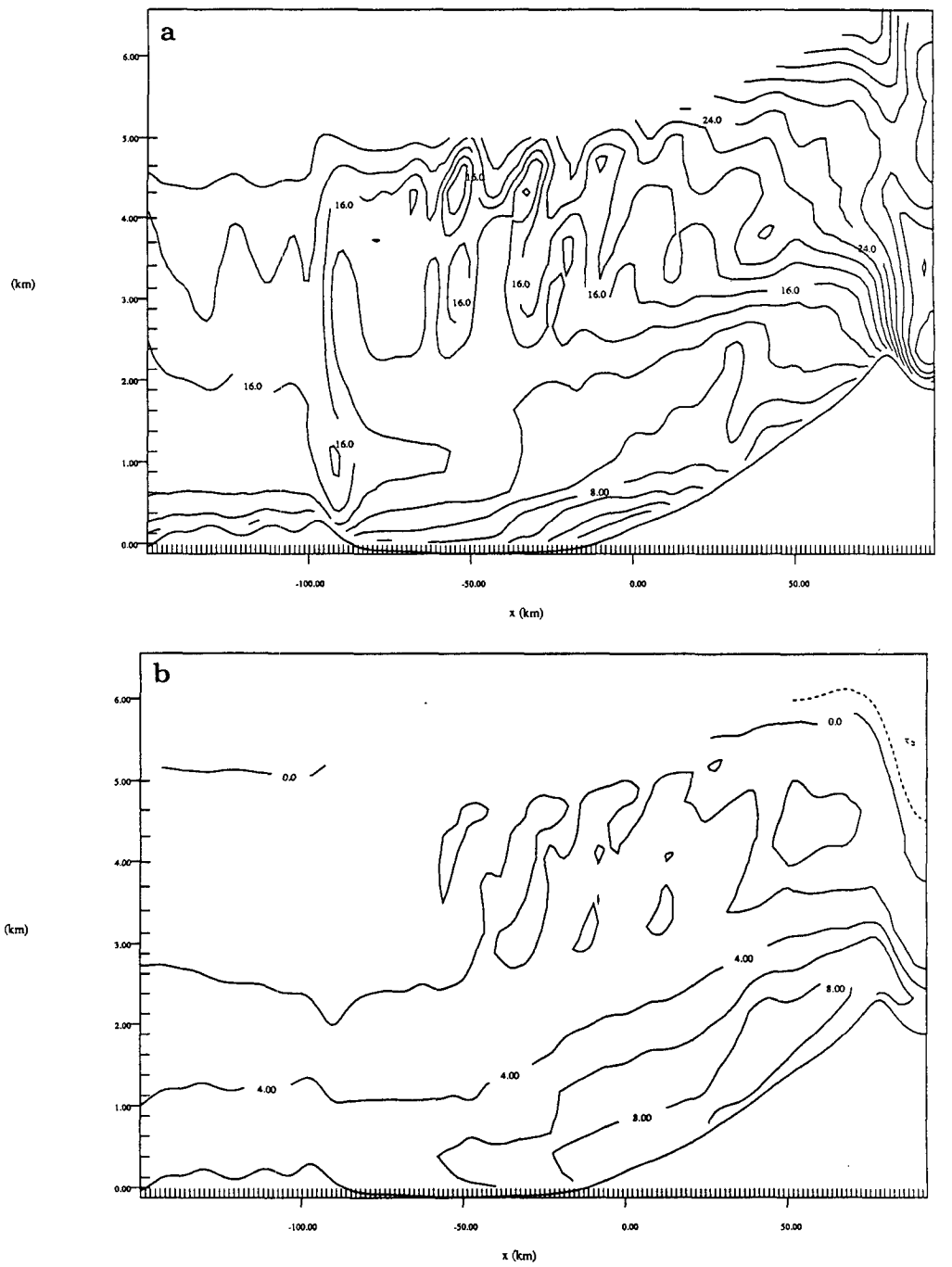

FIG. 8. Simulated wind and pressure fields for the simulation with melting not included of (a) u component of the wind, the contour interval is 2.0 m s^{-1}; (b) v component of the wind, the contour interval is 2.0 m s^{-1}; (c) pressure perturbation field, the contour interval is 0.4 mb. Solid lines are positive and dashed lines are negative. All fields shown at 6 h of simulation time. The abscissa and ordinate are in kilometers.

the melting layer that is located just below the 2 km MSL along the barrier. The pressure perturbation (Fig. 8b) fields are slightly different between the two experiments with positive pressure perturbations about 10% weaker along the barrier, attributing a 0.4-hPa pressure excess to the effects of melting. These results are not as dramatic as reported in previous studies. This case was a bit warmer than Marwitz's (1983) case study, so

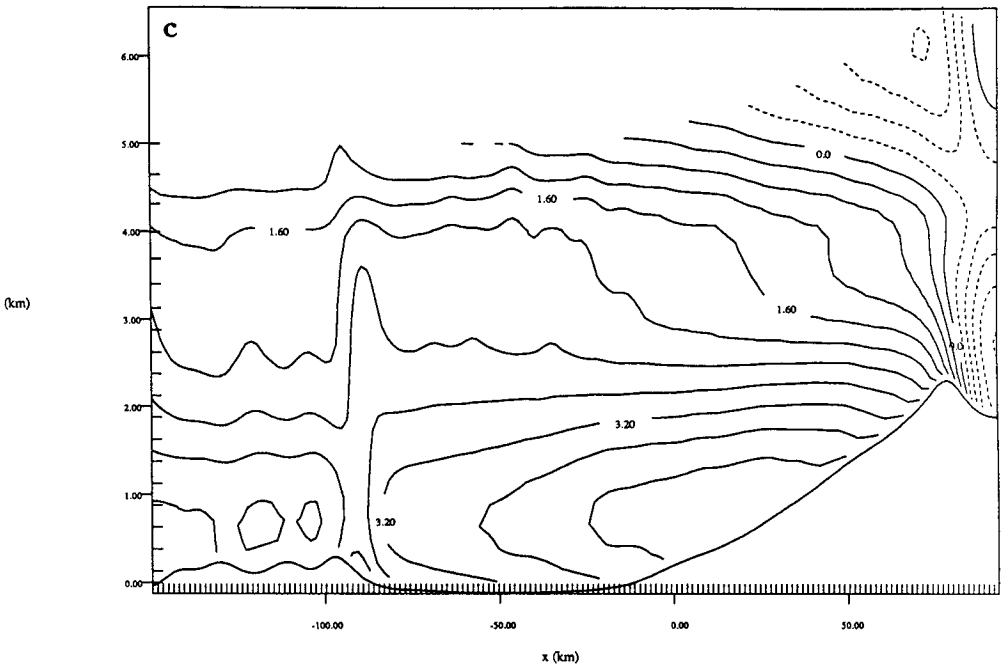

FIG. 8. (*Continued*)

that the diabatic response of melting may not have has as much impact on the flow fields in the lower levels. The dynamic feedback between melting and the flow fields appears to be case specific with the altitude of the melting level critical to the strength of this feedback.

d. Sensitivity to wind profile

This sensitivity experiment is initialized with the wind profile from Sheridan at 1500 UTC as shown in Fig. 3b. In all other respects, the simulation is the same as the control run. This experiment tests the model response to initialization with a representative input sounding. The Sheridan wind sounding, which represents the winds immediately west of the barrier, does not properly represent the winds at the inflow boundary of the model domain. This experiment illustrates the impact of selecting what would appear at first sight as the most representative sounding.

The predicted winds and pressure fields at 6 h for this sensitivity experiment are shown in Fig. 9. The u component of the wind (Fig. 9a) is more ageostrophic over the base of the barrier than in the control run with the winds reversing direction to a weak easterly return flow. The v component (Fig. 9b) shows a barrier jet oriented higher on the barrier than the control run. The magnitude of the simulated v component (20 m s^{-1}) is close to observed values. Since the simulation was initialized with a fairly strong v component, however, replication of observations does not necessarily indicate that the consistency of the dynamics are modeled correctly. The simulated pressure perturbations (Fig. 9c) are 25% less and situated farther up the barrier than the control run. The positive pressure perturbations are not as strong since the initialized cross-barrier flow was much weaker than the control run. The w field (Fig. 9d) is concentrated near the barrier crest and is weaker in response to the pressure field. The microphysical fields are quite similar to the control run in structure but magnitudes are much less since the cross-barrier winds are weaker, producing less condensate.

The precipitation distribution for this experiment (Fig. 10) shows a topography-dependent precipitation distribution with the peak value simulated at the top of the barrier. Since the orographic blocking developed high on the barrier forcing orographic ascent on the upper half of the barrier, the precipitation maximum was forced near the barrier crest. These results are inconsistent with the observations (see R92, Fig. 12) and the control run (Fig. 6) that exhibited a midmountain maximum in the precipitation, highlighting the importance of initializing with a wind profile, which is representative of the inflow boundary environment.

e. Sensitivity to Coriolis parameter

The Coriolis parameter forces the v component in 2D simulations. The v component, and specifically the barrier jet, is an observed characteristic of the orographic blocking occurring in this storm. The importance of the Coriolis forcing on other parameters,

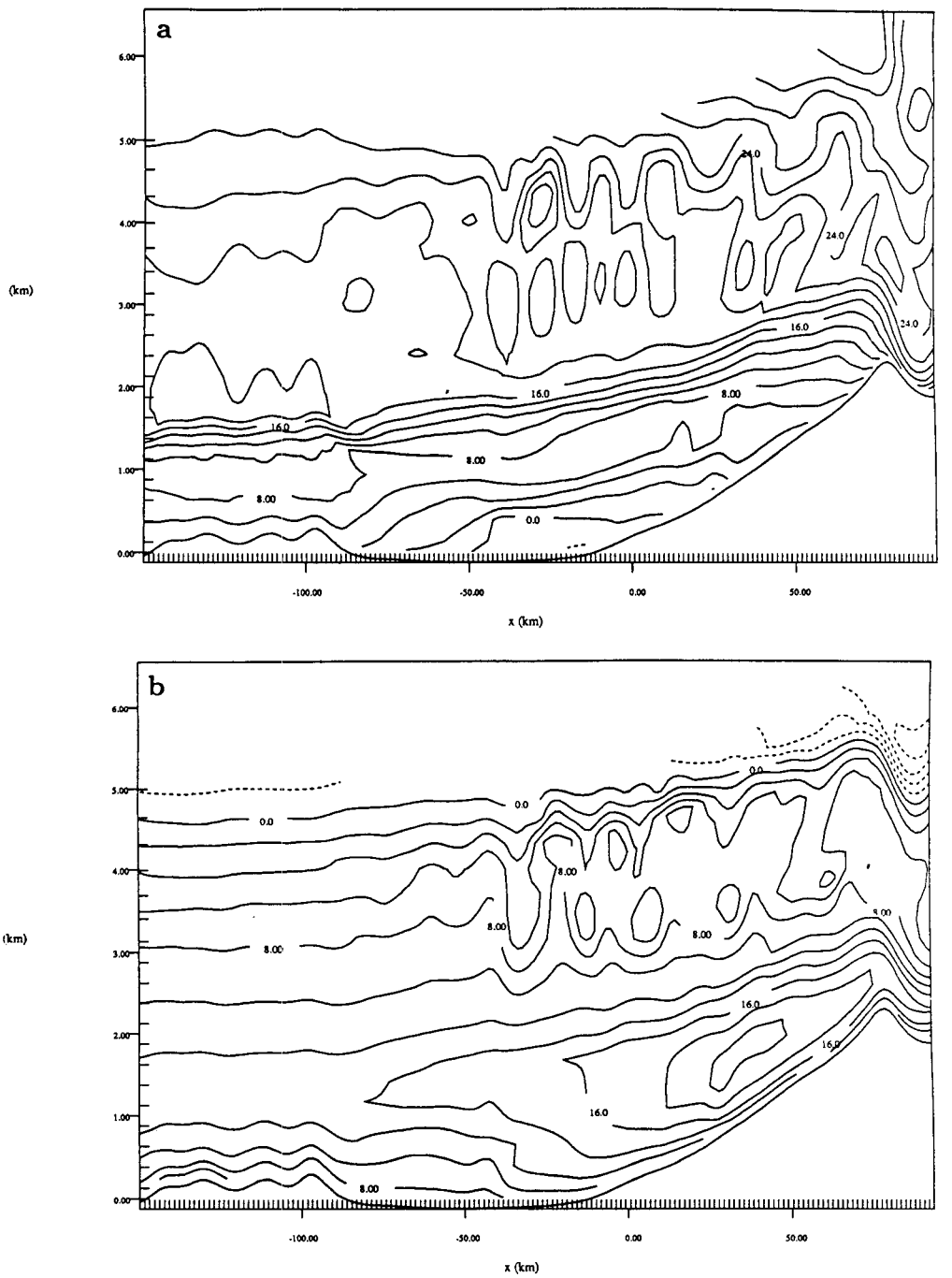

FIG. 9. Simulated wind and pressure fields for the simulation initialized with actual Sheridan sounding winds of (a) u component of the wind, the contour interval is 2.0 m s^{-1}; (b) v component of the wind, the contour interval is 2.0 m s^{-1}; (c) pressure perturbation field, the contour interval is 0.3 mb; (d) w component of the wind, the contour interval 0.2 m s^{-1}. The w component of the wind is windowed in more than the other fields for clarity. Solid lines are positive and dashed lines are negative. All fields shown at 6 h of simulation time. The abscissa and ordinate are in kilometers.

however, has not been examined. Therefore, in this sensitivity experiment the Coriolis parameter is deactivated.

The u-component wind (Fig. 11a) is more subgeostrophic over the windward side of the Sierra Nevada barrier with Coriolis turned off. As described earlier in

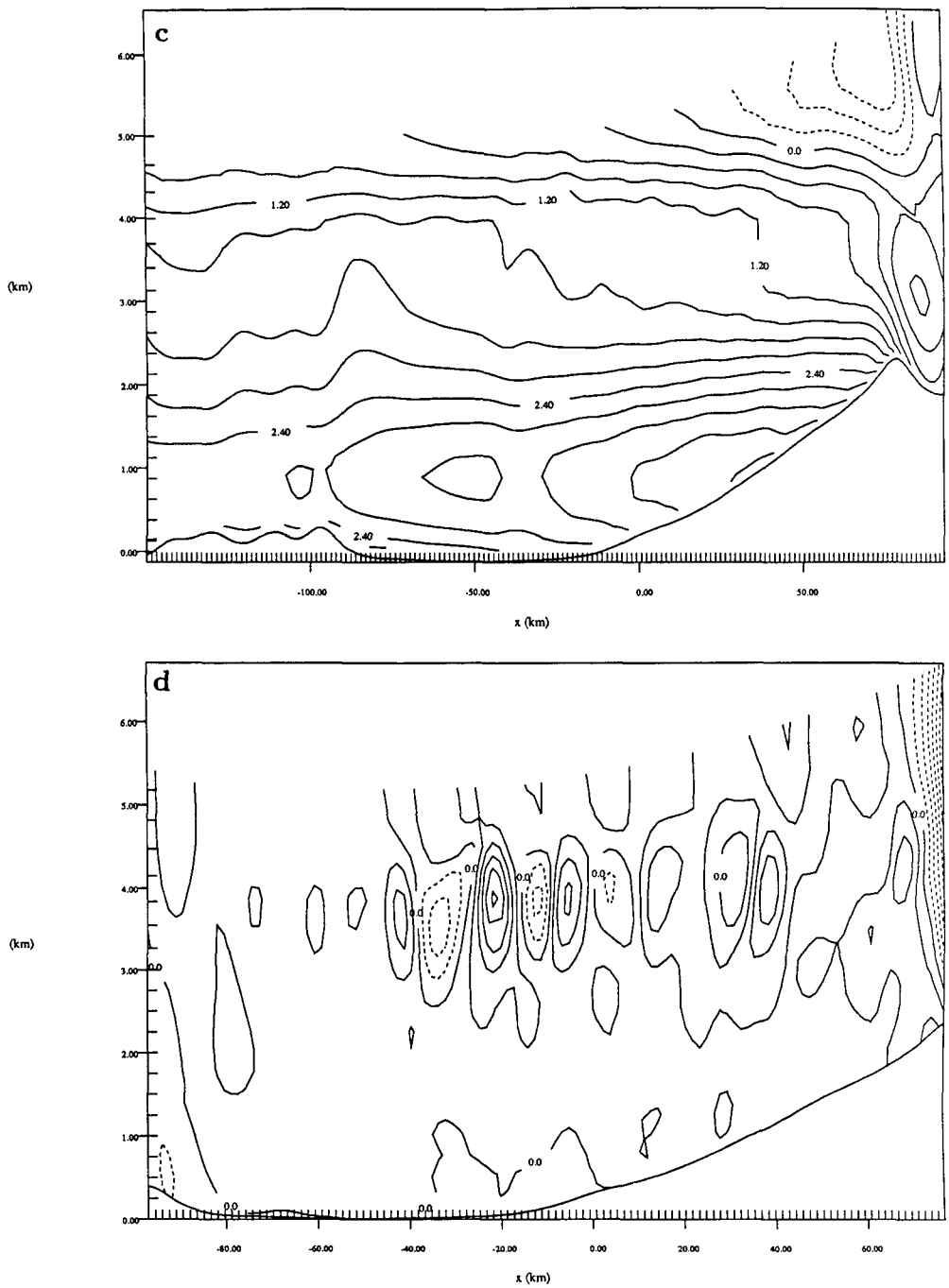

FIG. 9. (*Continued*)

the dry run experiment, the Coriolis force in the x direction accelerates the u component in the presence of v component. With the Coriolis force turned off, a source for the u component is removed hindering the flow over the barrier. The pressure perturbation field (Fig. 11b) exhibits a broad area of positive pressure perturbation against the barrier with a maximum value 33% less than in the control run. The w field exhibits widespread upward motions on the windward side of the Sierra Nevada with a weaker lee wave evident over the Coast Range (Fig. 11c).

Coriolis forcing affected the kinematic and pressure structure but the precipitation distribution (Fig. 12) was only slightly different from the control run. Coriolis

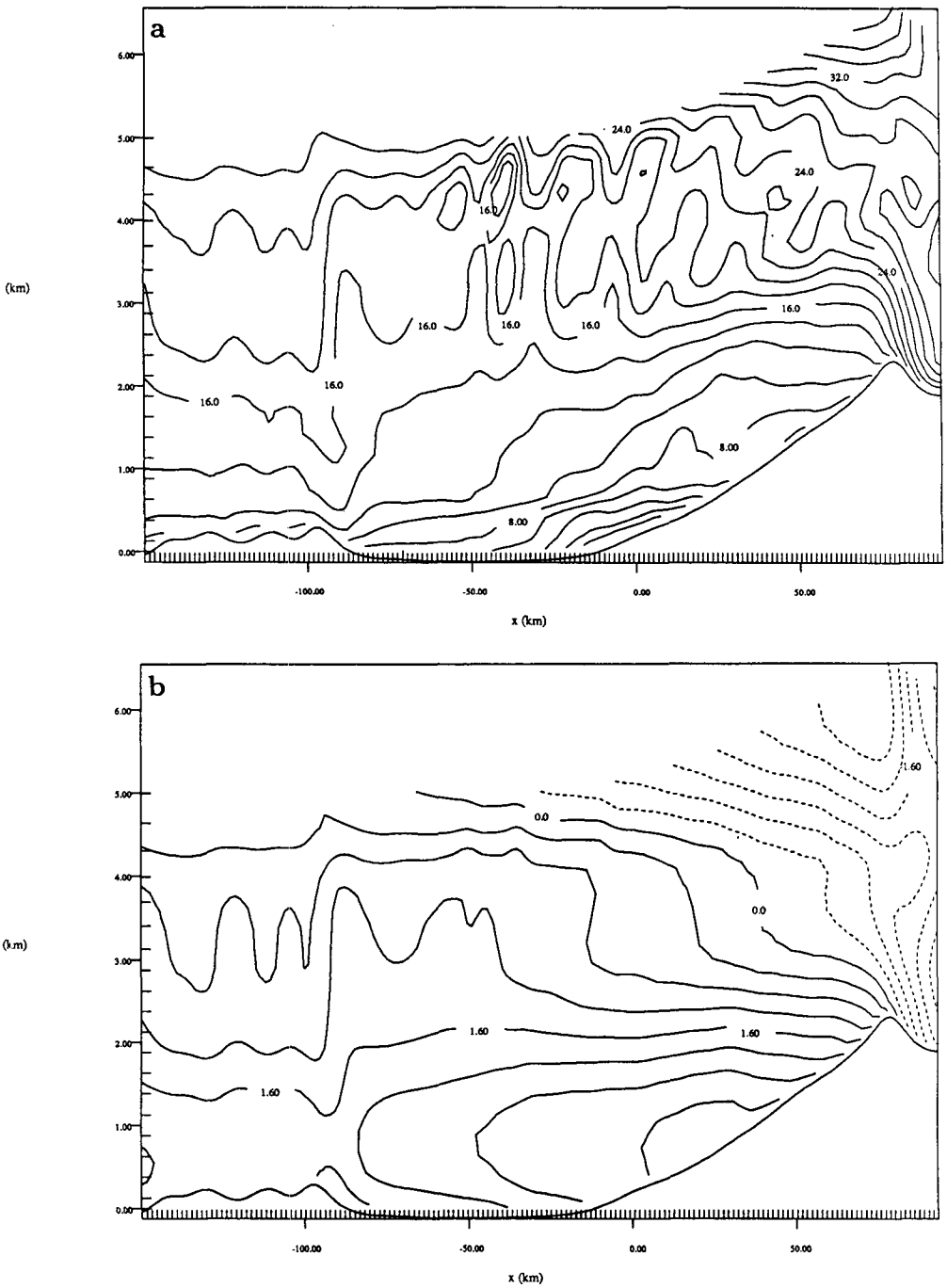

FIG. 11. Simulated wind and pressure fields for the simulation with Coriolis forcing not included of (a) u component of the wind, the contour interval is 2.0 m s^{-1}; (b) pressure perturbation field, the contour interval is 0.4 mb; (c) w component of the wind, the contour interval 0.2 m s^{-1}. The w component of the wind is windowed in more than the other fields for clarity. Solid lines are positive and dashed lines are negative. All fields shown at 6 h of simulation time. The abscissa and ordinate are in kilometers.

intense with pressure excesses nearly twice as large as the control run. The barrier jet also doubled compared to the control run since moist processes were absent in the dry run. The mechanisms responsible for the upstream wave structure were confirmed from the dry run. In the control run the mechanism that forced the flow upward upstream of the Sierra Nevada barrier was the orographic blocking, but the trigger responsible

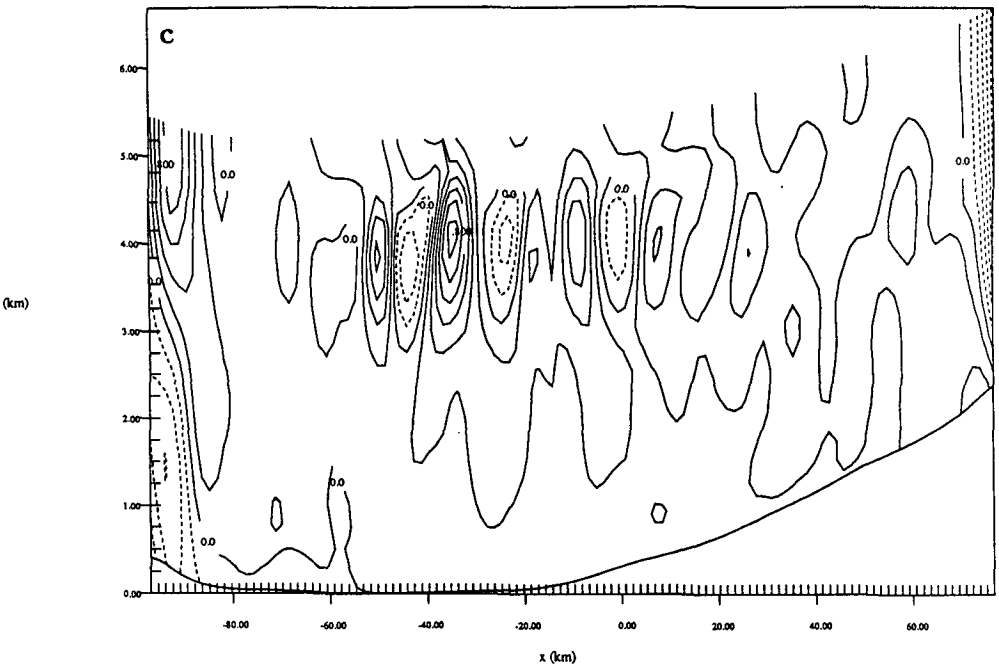

FIG. 11. (*Continued*)

for the cellular band was wet potential instability. In the dry simulation latent heat influences were absent and wet potential instability was not realized, suppressing the upstream wave structure in this simulation.

The sensitivity of the kinematic and mass fields to the diabatic influences of melting were not as dominant as in previous studies. The dynamic feedback between melting and the dynamic flow fields appears to be case specific. In this relatively warm case study, the melting layer may have been too high to allow a significant interaction between melting and the orographic blocking, which is centered low on the barrier.

The kinematic and mass fields showed sensitivity to Coriolis forcing, but the precipitation distribution was only slightly affected. The Coriolis forcing is also important in two-dimensional simulations because it allows prediction of another variable, the v component of the wind, to examine the dynamical consistency of the modeled flow.

Removing the Coast Range dramatically changed the pristine ice-crystal mass structure between 5 and 6 km MSL, indicating that a seeder–feeder production mechanism was triggered by the Coast Range. The effect on the precipitation distribution, however, was slight due, in fact, to the strong ambient winds present in this case. These strong winds advected the pristine crystals far downstream before settling into barrier precipitation processes occurred. In a weaker wind environment the Coast Range–induced seeder–feeder mechanism may produce a greater impact on precipitation. It is believed that the assumed monodispersed size spectrum of pristine ice crystals also exaggerated the horizontal advection of the pristine ice crystals.

The flow fields exhibited little sensitivity to the model microphysics. The precipitation distribution exhibited sensitivity to the graupel species being turned off. This sensitivity experiment showed that the removal of a process, such as graupel, is nearly compensated by the enhancement of other processes, such as rain and ag-

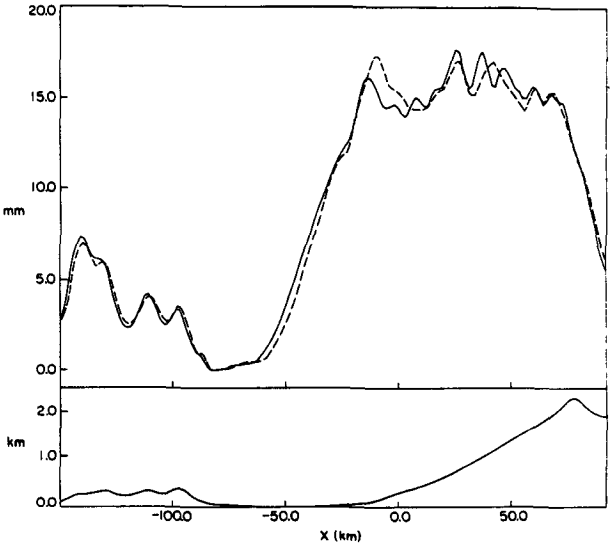

FIG. 12. Same as Fig. 10, except that the precipitation distribution for simulation with Coriolis forcing not included is dashed line.

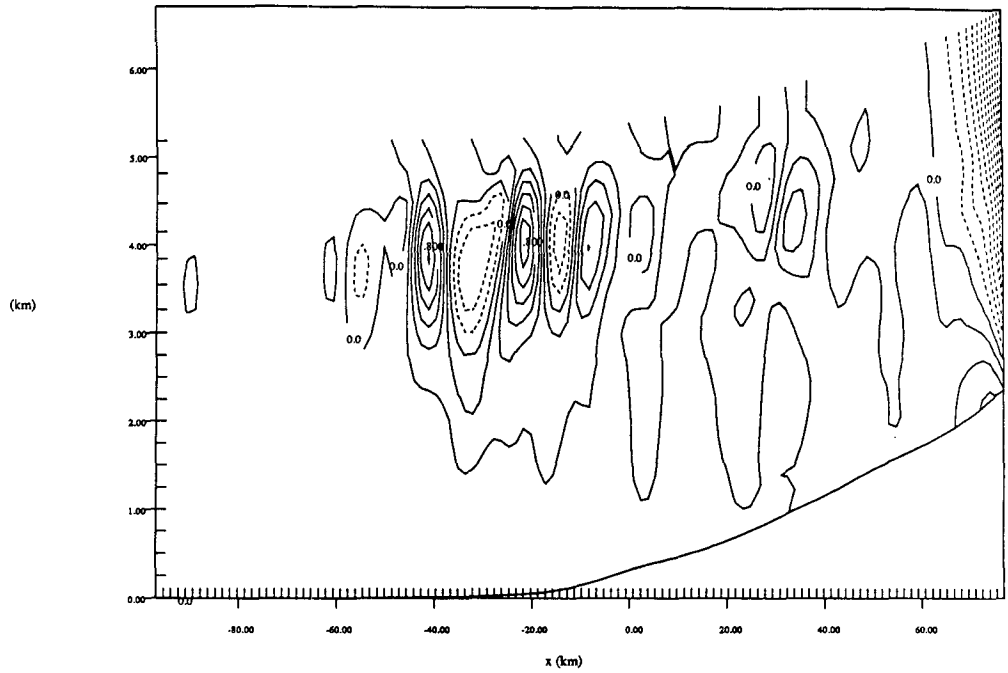

FIG. 13. The w-component field for the simulation with the Coast Range not included at 6 h of simulation time, the contour interval 0.2 m s^{-1}. The w component of the wind is windowed in more than the other fields for clarity. Solid lines are positive and dashed lines are negative. The abscissa and ordinate are in kilometers.

gregation. However, with more mass available for lower terminal velocity aggregates, a secondary peak resulted near the barrier crest. This shifting of the precipitation distribution is in response to the slower falling aggregates being advected farther downstream than the higher terminal velocity graupel particle.

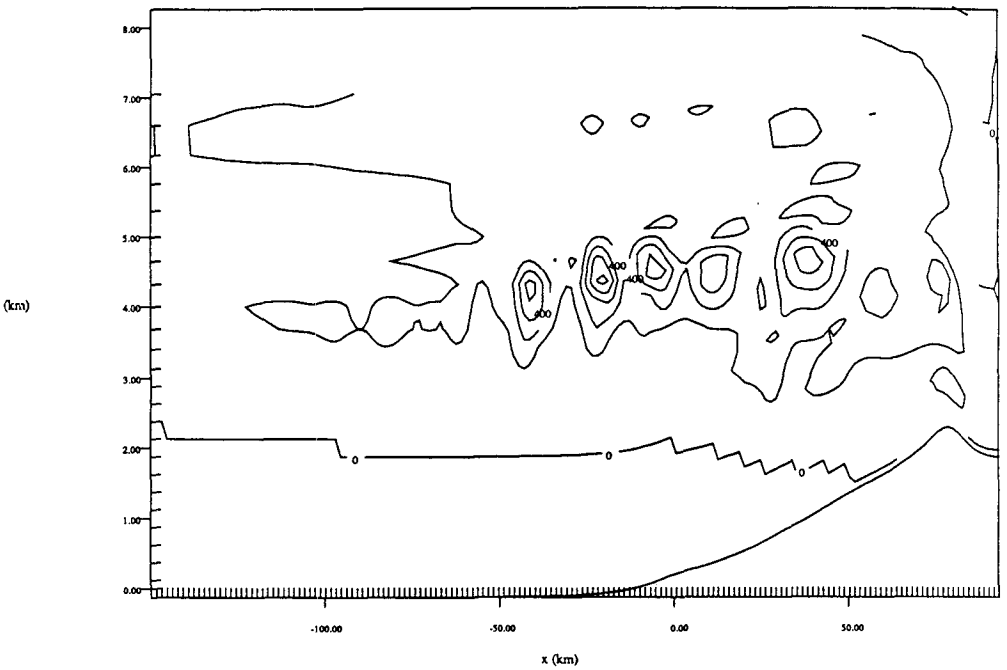

FIG. 14. The pristine ice-crystal mixing ratio field for the simulation with the Coast Range not included at 6 h of simulation time, the contour interval is 0.2 g kg^{-1} and the maximum value is 1.0 g kg^{-1}. The contour labels are 10^{3} g kg^{-1}. The abscissa and ordinate are in kilometers.

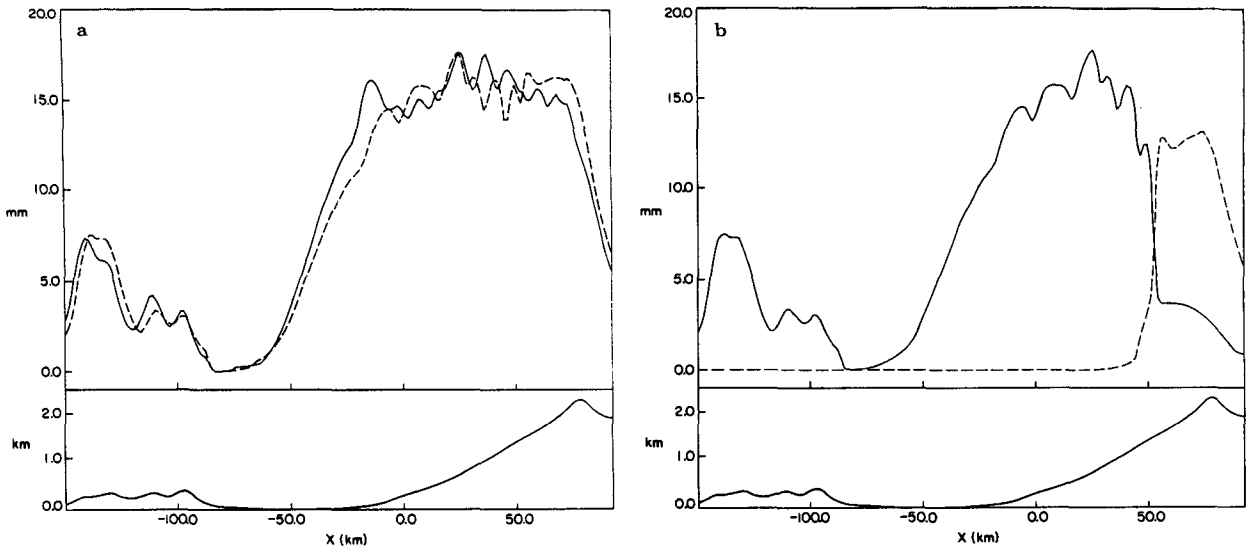

FIG. 15. (a) Precipitation distribution for the simulation with no graupel (dashed lines), and precipitation distribution for the control run (solid lines) for 3 h period with topography scaled below. (b) Precipitation distribution for no graupel simulation of (i) rain (solid lines); (ii) aggregates (dashed lines) for 3 h period with topography scaled below. The abscissa is in kilometers and the ordinate is total precipitation amount in millimeters.

The model showed a greater sensitivity to changing the graupel density from 0.45 to 0.9 g cm^{-3} and 0.1 g cm^{-3}. Increasing the density of graupel resulted in decreased residence time of graupel, which decreased the bulk graupel mass in the domain. Total precipitation over the barrier decreased by 4% and the amount of rain produced by melted graupel decreased dramatically. Decreasing the graupel density to 0.1 g cm^{-3} effectively created a graupel–snow hybrid with higher residence time, which produced greater overall graupel mass. Aggregates were practically eliminated due to the new hybrid species since any light riming of the aggregate particle would quickly convert it to graupel. Overall precipitation over the barrier increased by 7%.

Sensitivity of the precipitation distribution to secondary ice production due to riming was not apparent. Deposition–condensation freezing and contact nucleation appeared to dominate the nucleation modes in the model overwhelming any pristine crystals produced by secondary ice production.

TABLE 2. Precipitation analysis over upwind slope of barrier.

Experiment	Percent difference from control run	Percent frozen precipitation
Control run		34
Sensitivity to ambient wind	−35	39
No Coast Range	−1	34
Coriolis turned off	~0	34
No melting	−2	64
No graupel	−1	23
Graupel density = 0.9 g cm^{-3}	−4	40
Graupel density = 0.1 g cm^{-3}	+7	29
No secondary ice production	~0	34
CCN = 5 cm^{-3}	~0	33
CCN = 200 cm^{-3}	~0	34

These simulations suggest that quantitative precipitation forecasts are feasible with an explicit cloud microphysical model. To realistically simulate the spatial variations of precipitation, and to examine the sensitivity of varying the resolution of the fine grid, three-dimensional nested grid simulations will be conducted in Part II of this wintertime orographic precipitation case study. A three-dimensional simulation would also show the importance of the meridional transport of low-level moist air by the barrier jet and how this mesoscale feature influences the resultant precipitation distribution. This experiment has shown how critical it is to initialize with representative soundings. This problem was accentuated even more since a homogeneous initialization was employed. Therefore, initialization using an inhomogeneous objective analysis scheme will be conducted in Part II. Pristine ice-crystal concentrations appeared to be overpredicted by the nucleation modes currently present in the model. Work is needed to incorporate more recent research on ice nucleation into parameterizations, which should improve the prediction of primary and secondary ice production.

Acknowledgments. The authors wish to acknowledge Dr. Craig Tremback, Dr. Gregory Tripoli, and Dr. Robert Walko for their many helpful suggestions in applying the model. We also appreciate the cooperation of the SCPP personnel who provided field data and valuable insights on this case. Thanks are also extended

to Ray McAnelly for valuable suggestions. We are also grateful to Dr. James Bossert, Dr. Jerome Schmidt, Peter Olsson, and Johannes Verlinde for reviewing the manuscript. Brenda Thompson helped with processing the manuscript. This research was supported by the Army Research Office under Contract DAAL03-86-K-0175. Computations were performed at the National Center for Atmospheric Research (NCAR). NCAR is sponsored by the National Science Foundation.

REFERENCES

Anthes, R. A., and T. T. Warner, 1978: The development of hydrodynamic models suitable for air pollution and other mesometeorological studies. *Mon. Wea. Rev.*, **106,** 1045–1078.

Bergeron, T., 1949: The problem of artificial control of rainfall on the globe. II: The coastal orographic maxima of precipitation in autumn and winter. *Tellus,* **1,** 15–32.

——, 1965: On the low-level redistribution of atmospheric water caused by orography. *Supplement, Proc. International Conf. on Cloud Physics,* IUGG, WMO, Sci. Council of Japan, and Meteor. Soc. of Japan, Tokyo, 96–100.

Browning, K. A., 1985: Conceptual models of precipitation systems. *Meteor. Mag.,* **114,** 293–318.

——, and G. A. Monk, 1982: A simple model for the synoptic analysis of cold fronts. *Quart. J. Roy. Meteor. Soc.,* **108,** 435–452.

Cotton, W. R., and R. A. Anthes, 1989: *Storm and Cloud Dynamics.* Academic Press, 883 pp.

——, M. A. Stephens, T. Nehrkorn, and G. J. Tripoli, 1982: The Colorado State University three-dimensional cloud/mesoscale model—1982. Part II: An ice phase parameterization. *J. Rech. Atmos.,* **16,** 295–320.

——, G. J. Tripoli, R. M. Rauber, and E. A. Mulvihill, 1986: Numerical simulation of the effects of varying ice crystal nucleation rates and aggregation processes on orographic snowfall. *J. Climate Appl. Meteor.,* **25,** 1658–1680.

Durran, D. R., and J. B. Klemp, 1982a: On the effects of moisture on the Brunt–Väisälä frequency. *J. Atmos. Sci.,* **39,** 2152–2158.

——, and ——, 1982b: On the effects of moisture on trapped mountain lee waves. *J. Atmos. Sci.,* **39,** 2490–2506.

Flatau, P. J., G. J. Tripoli, J. Verlinde, and W. R. Cotton, 1989: The CSU-RAMS cloud microphysical module: General theory and code documentation. Atmospheric Science Paper No. 451, 88 pp. [Available from Colorado State University, Dept. of Atmospheric Science, Fort Collins, CO 80523.]

Fletcher, N. H., 1962: *Physics of Rain Clouds.* Cambridge University Press, 386 pp.

Gal-Chen, T., and R. C. J. Somerville, 1975a: On the use of a coordinate transformation for the solution of the Navier–Stokes equations. *J. Comput. Physics,* **17,** 209–228.

——, and ——, 1975b: Numerical solution of the Navier–Stokes equations with topography. *J. Comput. Physics,* **17,** 276–310.

Godske, C. L., T. Bergeron, J. Bjerknes, and R. C. Bundgaard, 1957: *Dynamic Meteorology and Weather Forecasting.* Amer. Meteor. Soc., 800 pp.

Hallett, J., and S. C. Mossop, 1974: Production of secondary ice particles during the riming process. *Nature,* **249,** 26–28.

Heggli, M. F., 1986: A ground based approach used to determine cloud seeding opportunity. *Proc., 10th Conf. on Weather Modification,* Arlington, VA, Amer. Meteor. Soc., 64–67.

Hobbs, P. V., 1978: Organization and structure of clouds and precipitation on the mesoscale and microscale in cyclonic storms. *Rev. Geophys. Space Phys.,* **16,** 741–755.

——, R. A. Houze, Jr., and T. J. Matejka, 1975: The dynamical and microphysical structure of an occluded frontal system and its modification by orography. *J. Atmos. Sci.,* **35,** 1542–1562.

Klemp, J. B., and R. B. Wilhelmson, 1978: The simulation of three-dimensional convective storm dynamics. *J. Atmos. Sci.,* **35,** 1070–1096.

——, and D. R. Durran, 1983: An upper boundary condition permitting internal gravity wave radiation in numerical mesoscale models. *Mon. Wea. Rev.,* **111,** 430–444.

Marwitz, J. D., 1983: The kinematics of orographic airflow during Sierra storms. *J. Atmos. Sci.,* **40,** 1218–1227.

——, K. Waight, B. Martner, and G. Gordon, 1985: Cloud physics studies in SCPP during 1984–1985. Report to Division of Atmospheric Resource Research, Bureau of Reclamation, U.S. Department of the Interior on Contract No. 2-07-81-V0256, 87 pp.

——, 1987: Deep, orographic storms over the Sierra. Part II: The precipitation processes. *J. Atmos. Sci.,* **44,** 174–185.

Meyers, M. P., 1989: An evaluation of the factors affecting wintertime quantitative precipitation forecasts in an explicit cloud model over mountainous terrain. Atmospheric Science Paper No. 450, M.S. thesis, Dept. of Atmospheric Science, Colorado State University, Fort Collins, CO 80523, 127 pp.

Orlanski, I., 1975: A rational subdivision of scales for atmospheric processes. *Bull. Amer. Meteor. Soc.,* **56,** 527–530.

Parish, T., 1982: Barrier winds along the Sierra Nevada mountains. *J. Appl. Meteor.,* **21,** 925–930.

Pierrehumbert, R. T., and B. Wyman, 1985: Upstream effects of mesoscale mountains. *J. Atmos. Sci.,* **42,** 977–1003.

Rauber, R. M., 1981: Microphysical processes in two stably stratified orographic cloud systems. Atmospheric Science Paper #337, 151 pp. Dept. Atmospheric Science, Colorado State University, Ft. Collins, CO 80523.

——, 1992: Microphysical structure and evolution of a central Sierra Nevada shallow orographic cloud system. *J. Appl. Meteor.,* **31,** 3–24.

Reynolds, D. W., and A. S. Dennis, 1986: A review of the Sierra Cooperative Pilot Project. *Bull. Amer. Meteor. Soc.,* **67,** 513–523.

Schwerdtfeger, W., 1974: Mountain barrier effect on the flow of stable air north of the Brooks Range. *Proc. 24th Alaskan Science Conf.,* Fairbanks, University of Alaska, 204–208.

——, 1975: The effect of the Antarctic Peninsula on the temperature regime of the Weddell Sea. *Mon. Wea. Rev.,* **103,** 45–51.

Smith, R. B., 1979: The influence of mountains on the atmosphere. *Advances in Geophysics,* Vol. 21, Academic Press, 87–230.

Smolarkiewicz, P. K., R. M. Rasmussen, and T. L. Clark, 1988: On the dynamics of Hawaiian cloud bands: Island forcing. *J. Atmos. Sci.,* **45,** 1872–1905.

——, and R. Rotunno, 1990: Low froude number flow past three-dimensional obstacles. Part II: Upwind flow reversal zone. *J. Atmos. Sci.,* **47,** 1498–1511.

Tripoli, G. J., and W. R. Cotton, 1982: The Colorado State University three-dimensional cloud/mesoscale model—1982. Part I: General theoretical framework and sensitivity experiments. *J. Rech. Atmos.,* **16,** 185–220.

——, and ——, 1989: Numerical study of an observed orogenic mesoscale convective system. Part 1: Simulated genesis and comparison with observations. *Mon. Wea. Rev.,* **117,** 273–304.